JGR Space Physics

RESEARCH ARTICLE
10.1029/2021JA029757

Electron Lifetimes and Diffusion Rates Inferred From ELFIN Measurements at Low Altitude: First Results

D. Mourenas[1,2], A. V. Artemyev[3], X. -J. Zhang[3], V. Angelopoulos[3], E. Tsai[3], and C. Wilkins[3]

[1]CEA, DAM, DIF, Arpajon, France, [2]Laboratoire Matière en Conditions Extrêmes, Paris-Saclay University, CEA, Bruyères-le-Châtel, France, [3]Department of Earth, Planetary, and Space Sciences, University of California, Los Angeles, CA, USA

Key Points:

- Electron lifetimes and diffusion rates inferred from trapped and precipitated fluxes measured by Electron Loss and Fields Investigation (ELFIN) agree with statistical models
- Electromagnetic ion cyclotron (EMIC) waves can strongly reduce electron lifetimes above 1–2 MeV throughout the outer radiation belt
- Atmospheric backscatter in conjugate regions likely contributes significantly to measured precipitated energetic electron fluxes

Correspondence to:
D. Mourenas,
didier.mourenas@cea.fr

Citation:
Mourenas, D., Artemyev, A. V., Zhang, X.-J., Angelopoulos, V., Tsai, E., & Wilkins, C. (2021). Electron lifetimes and diffusion rates inferred from ELFIN measurements at low altitude: First results. *Journal of Geophysical Research: Space Physics*, *126*, e2021JA029757. https://doi.org/10.1029/2021JA029757

Received 6 JUL 2021
Accepted 30 OCT 2021

Abstract In the radiation belts, energetic and relativistic electron precipitation into the atmosphere is expected to be mainly controlled over the long term by quasilinear pitch-angle scattering by whistler-mode and electromagnetic ion cyclotron waves. Accordingly, statistical electron lifetimes have been derived from quasilinear diffusion theory on the basis of multi-year wave statistics. However, the full consistency of such statistical quasilinear models of electron lifetimes with both measured electron lifetimes, spectra of trapped and precipitated electron fluxes, and wave-driven diffusion rates inferred from electron flux measurements, has not yet been verified in detail. In the present study, we use data from Electron Loss and Fields Investigation (ELFIN) mission CubeSats, launched in September 2018 in low Earth orbit, to carry out such comparisons between quasi-linear diffusion theory and observed electron flux variations. We show that statistical theoretical lifetime models are in reasonable agreement with electron pitch-angle diffusion rates inferred from the precipitated to trapped 100 keV electron flux ratio measured by ELFIN after correction for atmospheric backscatter, as well as with timescales of trapped electron flux decay independently measured over several days by ELFIN. The present results demonstrate for the first time a broad consistency between timescales of trapped electron flux decay, the pitch-angle distribution of precipitated electrons, and quasilinear models of wave-driven electron loss, showing the reliability of such statistical electron lifetime models parameterized by geomagnetic activity for evaluating electron precipitation into the atmosphere during not too disturbed periods.

1. Introduction

Energetic and relativistic electron fluxes in the Earth's radiation belts vary wildly over timescales ranging from minutes to weeks in response to solar activity, through various source and loss processes (Baker et al., 2014; Boynton et al., 2016, 2017; Glauert et al., 2014; Mourenas et al., 2019; Murphy et al., 2018; Thorne et al., 2013; Turner et al., 2014). The main loss mechanisms include magnetopause shadowing and outward radial diffusion by ultralow frequency (ULF) waves (Olifer et al., 2018; Ozeke et al., 2014; Pinto et al., 2020; Shprits et al., 2006), precipitation of relativistic (mainly $> 1-2$ MeV) electrons through pitch-angle scattering, or nonlinear scattering and trapping, by electromagnetic ion cyclotron (EMIC) waves (Blum et al., 2015; Grach & Demekhov, 2020; Li et al., 2007; Mourenas et al., 2016; Sandanger et al., 2007; Summers & Thorne, 2003; Thorne & Kennel, 1971; Usanova et al., 2014; Zhang et al., 2021), precipitation of 0.01–5 MeV electrons via pitch-angle diffusion, or fast nonlinear scattering, by whistler-mode chorus waves outside the plasmasphere (Artemyev et al., 2016; Hikishima et al., 2010; Horne & Thorne, 2003; Mourenas et al., 2014, 2018; Mozer et al., 2018; Ni et al., 2008), and precipitation of 0.01–5 MeV electrons via pitch-angle diffusion by hiss, lightning-generated, and VLF transmitter waves inside the plasmasphere (Agapitov et al., 2014; Breneman et al., 2015; Claudepierre et al., 2020; Lyons & Thorne, 1973; Ma et al., 2017; Mourenas et al., 2017; Ross et al., 2019). EMIC waves are often more effective than chorus or hiss in precipitating relativistic electrons with small equatorial pitch-angles (Li et al., 2007; Usanova et al., 2014), but intense chorus waves can also produce a rapid and bursty precipitation of energetic and relativistic electrons (Chen et al., 2020; Hikishima et al., 2010; Mozer et al., 2018). Finally, combined scattering by EMIC and chorus or hiss waves in the same or different magnetic local time (MLT) sectors can lead to fast dropouts of electron flux up to high equatorial pitch-angles (Li et al., 2007; Mourenas et al., 2016; Pinto et al., 2019; Zhang et al., 2017).

The lifetimes of high equatorial pitch-angle electrons have recently been studied throughout the plasmasphere, using electron flux data from the near-equatorial Van Allen Probes, showing a good agreement with quasilinear models of hiss and EMIC wave-driven pitch-angle diffusion (Mourenas et al., 2017; Pinto et al., 2019; Zhang et al., 2017). However, it would be important to similarly examine the lifetimes of small equatorial pitch-angle electrons near the loss cone, to verify the prediction from quasi-linear diffusion theory that the full electron pitch-angle distribution should asymptotically decay as a whole with the same characteristic timescale (Kennel & Petschek, 1966; Meredith et al., 2009; Schulz & Lanzerotti, 1974).

Another key result of quasi-linear theory is that the ratio of precipitated over trapped electron fluxes should be determined by the diffusion rate at the loss cone edge (Kennel & Petschek, 1966). The latter result has been checked during approximate conjunctions between low-altitude Polar Orbiting Environmental Satellites (POES) measuring precipitated and trapped electron fluxes and the high-altitude Van Allen Probes measuring chorus waves near the equator (Li et al., 2013). Recently, Reidy et al. (2021) have also provided for the first time a comparison between electron diffusion rates inferred, using quasilinear theory, from precipitated to trapped electron flux ratios measured by POES, and statistical models of chorus wave-driven diffusion rates. Such a comparison would be worth performing again using newer spacecraft instruments with better energy and pitch-angle resolution because it can directly show whether models of electron precipitation based on statistical electron lifetimes (Aryan et al., 2020; Mourenas et al., 2017) can be reliably used for predicting the resulting modifications in the middle and upper atmosphere, such as ozone destruction (Seppälä et al., 2018). In addition, the full pitch-angle electron distribution shape measured within the loss cone would be worth comparing with predictions from quasilinear theory, to assess the accuracy of theory in describing the fine structure of the precipitated electron flux. A precise knowledge of the pitch angle distribution of precipitated electrons is indeed critical for accurately evaluating the energy deposition profile in the atmosphere (Marshall & Bortnik, 2018; Pettit et al., 2019).

However, the loss cone is smaller than 5° at the equator at adiabatically invariant L-shell $L^* > 4$. Therefore, it cannot be easily resolved by near-equatorial spacecraft. In contrast, the loss cone becomes much wider at low altitude (≈65° at 450 km), potentially enabling highly resolved measurements of both trapped and precipitating electron fluxes. Previous low altitude missions did not have a sufficient pitch-angle resolution, or provided only a single measurement within the loss cone of precipitated particles (Li et al., 2013), precluding a full characterization of the loss cone and an accurate assessment of the importance of atmospheric backscatter (Davidson & Walt, 1977; Marshall & Bortnik, 2018; Selesnick et al., 2004). However, the Electron Loss and Fields Investigation with a Spatio-Temporal Ambiguity-Resolving option (ELFIN) mission, launched in September 2018, provides a golden opportunity to finally carry out all the above-discussed comparisons between quasilinear wave-driven diffusion theory and observed electron flux variations (Angelopoulos et al., 2020).

The ELFIN mission consists of two identical 3-Unit CubeSats launched on nearly circular ∼90 min low-altitude (450 km) orbits with 93° inclination (Angelopoulos et al., 2020). Each spinning satellite (with 3 s spin period) carries an energetic particle detector for electrons (EPDE) measuring $0.05 - 5$ MeV electrons in 16 channels with energy resolution $\Delta E/E < 40\%$ and pitch-angle resolution <25°, a similar detector of $0.05 - 5$ MeV ions (EPDI), as well as a fluxgate magnetometer (FGM) recording magnetic field waves from DC to 5 Hz Nyquist with $<0.3\ \mathrm{nT}/\sqrt{(Hz)}$ noise. The spin axis of each satellite is maintained perpendicular to the orbit plane, allowing a full pitch-angle resolution of electrons twice per spin. To prevent a contamination of EPDE measurements by penetrating particles, detectors are in a vault with Ta (3 mm) plus Al (9 mm) walls, with apertures comprising phosphor-bronze knife-edge collimators (Angelopoulos et al., 2020). The expected signal-to-noise ratio is 10:1 in a realistic ion and electron environment, and coincidence logic further improves this ratio by a factor of 10 (also suppressing side-penetrating background). Therefore, the two ELFIN-A and ELFIN-B spinning CubeSats carry energetic electron detectors with a full 360° field of view and a sufficient pitch-angle resolution to allow, for the first time, all the above-listed comparisons between measured electron fluxes and quasilinear diffusion models.

In the next section, we compare electron flux decay rates measured by ELFIN during moderately disturbed periods with statistical models of electron lifetimes, finding a good agreement. In the third section, we further show that electron pitch angle and energy spectra within and near the loss cone are similarly consistent

with expectations from quasilinear theory and statistical wave models, provided that atmospheric backscatter is taken into account.

2. Maps of Electron Lifetimes From $L^* = 3.0$ to 6.6

2.1. Lifetime Inference From Low-Altitude Electron Flux

The quasilinear theory of electron pitch-angle diffusion by whistler-mode or electromagnetic ion cyclotron (EMIC) waves of not too high amplitude or not too high coherency indicates that the pitch-angle distribution of electrons interacting with such waves should rapidly assume a time-asymptotic (or steady-state) shape, corresponding to the lowest-order eigenmode of the Fokker-Planck diffusion equation (Schulz & Lanzerotti, 1974). This initial, rapid evolution of the electron pitch-angle distribution (confirmed by numerical simulations, see Meredith et al., 2009) occurs over timescales much smaller (typically ~10 times smaller) than the timescale of asymptotic electron flux decay τ_L, called lifetime (Schulz & Lanzerotti, 1974).

Subsequently, the electron pitch-angle distribution shape remains fixed (as determined by the pitch-angle diffusion rate $D_{\alpha\alpha}(\alpha)$, with α the equatorial pitch-angle) and decays exponentially as a whole with the decay timescale τ_L (Meredith et al., 2009; Schulz & Lanzerotti, 1974). During this asymptotic stage of exponential decay, the pitch-angle distribution shape in the vicinity and inside the bounce loss cone is fully determined by the diffusion rate $D_{\alpha\alpha}(\alpha_{LC})$ at the bounce loss cone angle α_{LC} (Kennel & Petschek, 1966; Li et al., 2013), and the whole pitch-angle distribution shape, both outside and inside the loss cone, remains fixed. Therefore, the trapped electron flux measured at low altitude by ELFIN slightly above α_{LC} should decay with the same characteristic timescale τ_L as the whole pitch-angle distribution.

But trapped electrons measured by ELFIN are less than a fraction of degree above the bounce loss cone angle α_{LC} (Angelopoulos et al., 2020). This mainly corresponds to quasi-trapped electrons with pitch-angles above the longitudinally averaged α_{LC} but below the drift loss cone angle α_{DLC}, defined as the maximum bounce loss cone angle reached at South Atlantic Anomaly (SAA) longitudes (Schulz & Lanzerotti, 1974; Tu et al., 2010). On a given L^* shell, azimuthally drifting quasi-trapped electrons with $\alpha < \alpha_{DLC}$ are lost in the atmosphere when they cross SAA longitudes. Next, the drift loss cone is progressively refilled over $\alpha_{LC} < \alpha < \alpha_{DLC} \simeq 1.2\alpha_{LC}$ by wave-driven pitch-angle diffusion along the azimuthal electron drift (Schulz & Lanzerotti, 1974). At longitudes sufficiently far eastward from the SAA, this refilling gives a quasi-trapped to trapped (at $\alpha = \alpha_{DLC}$) electron flux ratio near unity, as confirmed by SAMPEX observations (Tu et al., 2010). This refilling occurs closer eastward from the SAA for lower energy (<300 keV) electrons, due to their stronger pitch-angle diffusion and slower azimuthal drift (Mourenas et al., 2012; Schulz & Lanzerotti, 1974; Tu et al., 2010), and also at 0–10 MLT where chorus-driven diffusion is stronger (Aryan et al., 2020). In principle, this allows us to use the trapped or quasi-trapped (hereafter simply called trapped) electron flux measured at a fixed longitude sufficiently far eastward from the SAA (or equivalently at a fixed MLT since ELFIN is sun-synchronous) to determine electron lifetimes τ_L under the assumption of exponential decay of their whole pitch-angle distribution. At such a longitude, the pitch-angle distribution shape near and below α_{LC} is determined by $D_{\alpha\alpha}(\alpha_{LC})$ (Kennel & Petschek, 1966).

Figure 1 shows examples of trapped and precipitated 0.05–3 MeV electron fluxes measured by ELFIN-A during two successive orbits on September 5 and 6, 2020, as a function of time, L^*, and MLT. The first patch of high electron fluxes up to 2–3 MeV at $L^* = 4$–7 in Figure 1(a1,b1) corresponds to the outer radiation belt and the second patch of high fluxes up to 0.5 MeV at $L^* < 2.5$–3 to the inner radiation belt, with the slot of reduced fluxes in-between them (Lyons & Thorne, 1973; Mourenas et al., 2017; Schulz & Lanzerotti, 1974). At $L^* \sim 4.5$–6.0, trapped electron fluxes are much larger near 0:30 MLT in Figure 1(a1), corresponding to magnetic longitudes ~260° far from the SAA, than near 3:30 MLT in Figure 1(a2), corresponding to magnetic longitudes ~300° inside the SAA. The corresponding local pitch-angle distributions are displayed in Figures 1c and 1d, showing the presence of both precipitated electrons and electrons backscattered by the atmosphere inside the loss cone.

To ensure that we deal with the asymptotic stage of exponential flux decay, we select periods satisfying three different sets of conditions. First, we focus on moderately disturbed periods starting a few days after a geomagnetic storm, or just after strong substorms. Such strong disturbances are expected to increase electron fluxes via injections from the plasma sheet and/or via electron acceleration by chorus or ULF

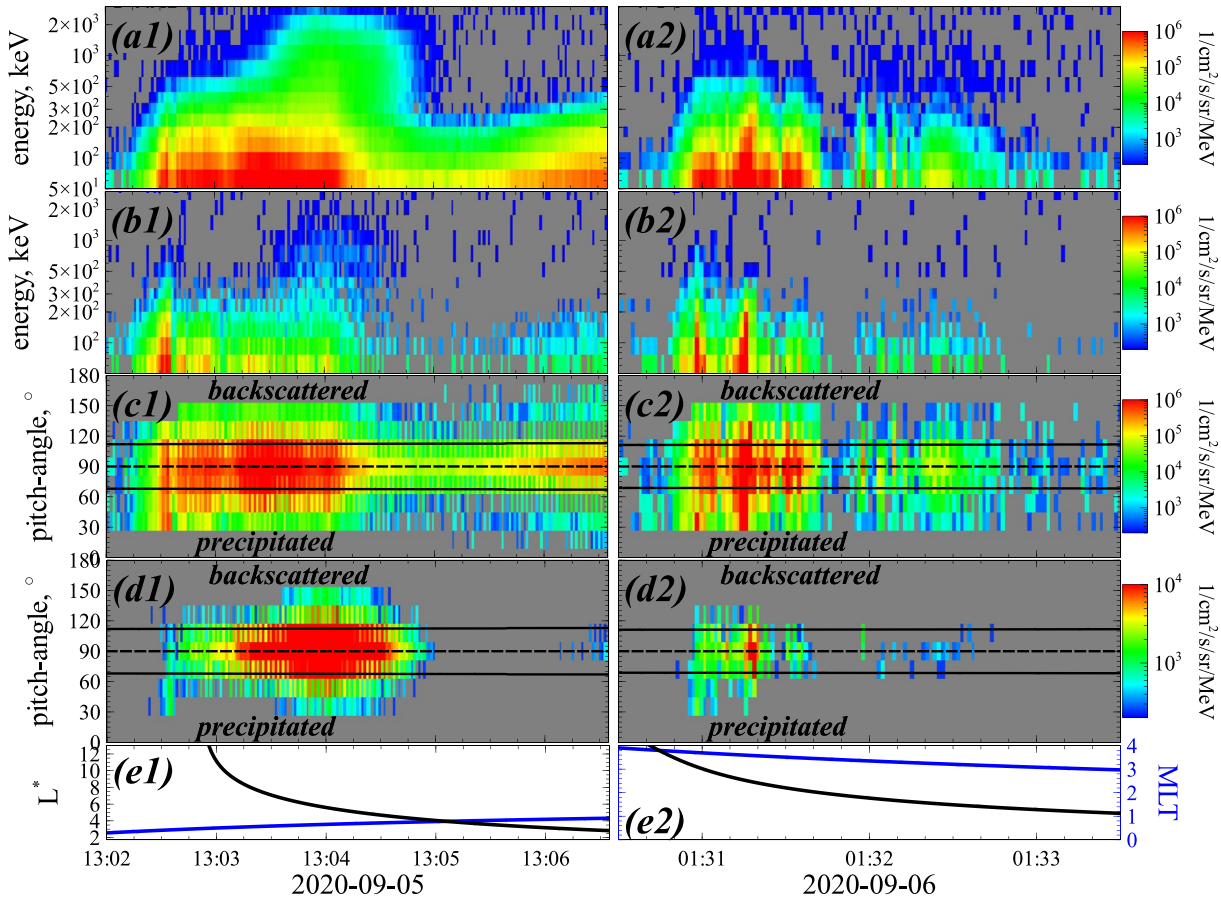

Figure 1. Electron fluxes measured by Electron Loss and Fields Investigation (ELFIN)-A as a function of time during two successive orbits on September 5–6, 2020. (a) Trapped flux of 0.05–3 MeV electrons, (b) precipitated flux of 0.05–3 MeV electrons, (c) local pitch-angle distribution of 50–150 keV electrons, (d) local pitch-angle distribution of 350–1000 keV electrons. (e) L^* (black) and magnetic local time (MLT) (blue). Horizontal lines in (c and d) show the loss cone edge. Gray bins correspond to instrument noise (~3 counts/s).

waves (Mourenas et al., 2017, 2019; Murphy et al., 2018; Ozeke et al., 2014; Thorne et al., 2013; Turner et al., 2015, 2017), providing favorable conditions for subsequent observations of electron flux decay. The *Dst* index is required to remain higher than −21 nT and to decrease by less than 5 nT, or increase by less than 9 nT, between the start and end of the selected periods, corresponding to a negligible adiabatic variation of electron energy (Kim & Chan, 1997) for an energy bin width $\Delta E/E \simeq 30\%$ at $L^* < 6.6$. Additional requirements are as follows: hourly interplanetary magnetic field component $B_z \geq -5$ nT, solar wind dynamic pressure *P*dyn < 4 nPa, and *Kp* < 3.5 during these whole periods and the preceding day. This should prevent the presence of other phenomena that could significantly modify electron fluxes, such as sudden electron loss (dropouts) at $L^* < 6.6$ caused by magnetopause shadowing and outward radial diffusion (Boynton et al., 2016, 2017; Mourenas et al., 2019; Olifer et al., 2018; Pinto et al., 2020; Shprits et al., 2006), significant electron injections (Turner et al., 2017), inward radial diffusion or local chorus-wave driven electron acceleration (Ma et al., 2015; Ozeke et al., 2014; Thorne et al., 2013; Turner et al., 2014, 2015), or non-linear effects from intense chorus waves (Gan et al., 2020; Hikishima et al., 2010; Kitahara & Katoh, 2019; Mourenas et al., 2018; Tao et al., 2012). Second, we investigate only the region $L^* \sim 3.5$–6.6 and select periods starting after at least ~1 day of initial decay of the 100–500 keV electron flux observed by ELFIN. After such an initial ~1-day decay, the asymptotic stage of exponential flux decay should have been reached for typical asymptotic lifetimes $\tau_L \sim 1$–10 days of ~0.1–2 MeV electrons at $L^* \sim 3.5$–6.6 in the presence of hiss, chorus, and EMIC waves during moderately disturbed periods (Aryan et al., 2020; Meredith et al., 2009; Mourenas et al., 2016, 2017; Schulz & Lanzerotti, 1974). Third, the selected periods must last two days or more, allowing precise measurements of trapped electron flux decay at longitudes sufficiently far from the SAA, and we check that this decay is approximately exponential. Figure 2 shows trapped electron fluxes measured

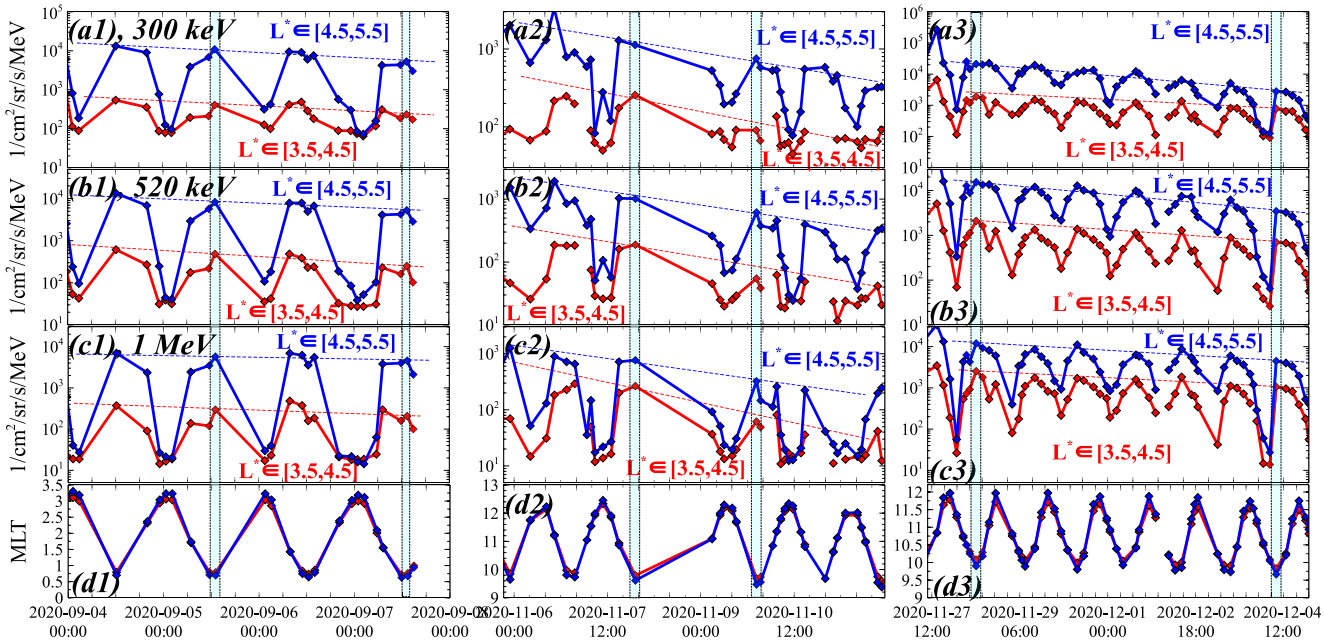

Figure 2. (a1, a2, a3) Trapped 300 keV electron flux measured by Electron Loss and Fields Investigation (ELFIN) at $L^* = 4.5–5.5$ (blue) and at $L^* = 3.5–4.5$ (red) during the three time intervals of 2020 examined in this study. The start and end of the selected periods are indicated by light blue vertical lines. Blue and red dotted lines show exponential decays. (b1, b2, b3) Same as (a1, a2, a3) for 520 keV electrons. (c1, c2, c3) Same as (a1, a2, a3) for 1 MeV electrons. (d1, d2, d3) Magnetic local time (MLT) of measurements.

by ELFIN in two L^*-shell ranges as a function of time, for different electron energies, during the three time intervals selected for this study. It demonstrates an approximately exponential decay of the maximum flux measured at a similar MLT (and longitude) over 3–6 days for the three selected periods.

2.2. Statistical Models of Theoretical Electron Lifetimes Controlled by Wave-Driven Scattering

Electron lifetimes τ_L directly obtained from trapped electron flux measurements on board ELFIN (assuming exponential decay) can be compared with statistical models of theoretical electron lifetimes, obtained using quasilinear diffusion theory and wave and plasma parameters from spacecraft statistics. Inside the plasmasphere (for $3 < L^* < \min[L_{pp}, 5]$), quasilinear diffusion by mostly incoherent and moderate amplitude whistler-mode hiss and lightning-generated waves (Gao et al., 2014; He et al., 2021; Li et al., 2015) and moderate amplitude hydrogen-band EMIC waves (Kersten et al., 2014; Zhang et al., 2016) mainly determines electron lifetimes (Glauert et al., 2014; Lyons & Thorne, 1973; Ma et al., 2015; Mourenas et al., 2017; Pinto et al., 2019). In the plasmasphere, a statistical model of theoretical electron lifetime τ_L (Mourenas et al., 2017; Zhang et al., 2017) is given by:

$$\tau_L \ [\text{day}] \approx R_{EMIC} \cdot \tau_{L,0} \tag{1}$$

where the lifetime $\tau_{L,0}$ due to hiss waves alone is given by

$$\begin{aligned} \tau_{L,0} \ [\text{day}] &\approx \tau_0 (p^{3/2}\gamma) \ \text{ for } \ p > 1.2p_0 \\ \tau_{L,0} \ [\text{day}] &\approx \tau_0 \frac{p_0^{11/2}\gamma_0}{2.4\, p^4} \ \text{ for } \ p < 0.75p_0 \\ \tau_{L,0} \ [\text{day}] &\approx \tau_0 (1.4\, p_0^{3/2}\gamma_0) \ \text{ for } \ 0.75p_0 < p < 1.2p_0 \end{aligned} \tag{2}$$

with

$$\tau_0 = \frac{(L^*)^2\,\eta^{7/9}}{40\,Kp\exp(-(L^*-3.2)^2/2)},$$
$$R_{EMIC} = \frac{\cos^2\alpha^* + 2\ln(\sin\alpha^*)}{\cos^2\alpha_{LC} + 2\ln(\sin\alpha_{LC})}, \quad (3)$$
$$\alpha^* = \min\left[\max\left(\alpha_{LC}, \alpha_{\max}^{EMIC}\right),\ 50^\circ\right]$$

with $p_0 = 10^{3/2}/(\eta^{1/2}[L^*]^{5/2})$, γ the Lorentz factor, $\gamma_0^2 = p_0^2 + 1$, and where lifetimes are provided as a function of the *Kp* index. This lifetime model, which includes additional effects from hydrogen-band EMIC waves via the factor $R_{\mathrm{EMIC}} \leq 1$, has been validated against numerical simulations for electron momentum (normalized to $m_e c$ with m_e the electron mass and c the speed of light) $p > p_0/5$ and $L^* < 5$ (Mourenas et al., 2017; Zhang et al., 2017). Hydrogen-band EMIC waves are assumed to possess the same characteristics (notably an upper cutoff frequency at ≃0.45 times the proton gyrofrequency) over $L^* \sim 3.5$–6.6 as discussed in Mourenas et al. (2017), except for a higher amplitude at higher $L^* > 5$ in agreement with EMIC waves statistics (Kersten et al., 2014; Mourenas et al., 2016; Zhang et al., 2016). Cyclotron resonance of electrons with such EMIC waves is possible up to a maximum equatorial pitch-angle $\alpha_{\max}^{EMIC} \simeq \cos^{-1}(\min[1, 8/(\eta^{1/2}(L^*/2)^{1.4}[E^2+E]^{1/2})])$ (Mourenas et al., 2016, 2017; Summers & Thorne, 2003), with E the electron energy in MeV and η the plasma density (in plasmasphere or plume) normalized to model plasmaspheric density (Ozhogin et al., 2012). Such EMIC waves are assumed to occur either inside the plasmasphere or in a plasmaspheric plume, in some limited MLT sector generally located around 9–21 MLT (Kersten et al., 2014; Zhang et al., 2017), with a similar plasma density dependence on L^* as inside the plasmasphere (Ozhogin et al., 2012) and with an ion composition of ∼85%–95% protons and a few percents of helium or oxygen ions (Kersten et al., 2014; Mourenas et al., 2017).

Outside the plasmasphere (for $3.5 < L_{\mathrm{pp}} < L^* < 6.6$) and during not too disturbed periods, quasi-linear diffusion by moderate amplitude (< 150 pT) short packets of lower-band chorus waves (Zhang et al., 2019) and not-too-high amplitude hydrogen-band EMIC waves (Kersten et al., 2014; Zhang et al., 2016) likely determines electron lifetimes over days to weeks (Glauert et al., 2014; Mourenas et al., 2016; Tao et al., 2012; Zhang et al., 2017, 2019; Zhang, Agapitov, et al., 2020). Outside the plasmasphere, a statistical model of theoretical electron lifetime τ_L, appropriate for periods with 100 < AE(nT)< 300, can be obtained (Aryan et al., 2020; Zhang et al., 2017) by simply replacing $\tau_{L,0}$ in Equation 1 by:

$$\tau_{L,0}\ \ [\mathrm{day}] \simeq \frac{200\,\gamma\,p^{3/2}}{(28.9 - 2.2L^*)^2\,(L^*/6.6)^{3/2}} \quad (4)$$

where $\tau_{L,0}$ given by Equation 4 is the electron lifetime due to pitch-angle scattering by chorus waves alone (Aryan et al., 2020).

The two above statistical models of electron lifetimes take into account the possible combined effects of whistler-mode waves and hydrogen-band EMIC waves present in different MLT sectors, which may scatter even high equatorial pitch-angle electrons toward the loss cone (Mourenas et al., 2016, 2017; Zhang et al., 2017). Such lifetime models rely on years-long statistics of plasmaspheric hiss and lightning-generated waves (Agapitov et al., 2013, 2014; Artemyev et al., 2013; Li et al., 2015), chorus waves (Agapitov et al., 2018; Aryan et al., 2020), and hydrogen-band EMIC waves (Kersten et al., 2014; Zhang et al., 2016) provided by CRRES, Akebono, Cluster satellites, and the Van Allen Probes. The plasma density is taken from statistical models of plasmaspheric density (Ozhogin et al., 2012) or trough density (Sheeley et al., 2001).

2.3. Comparisons Between Lifetimes Inferred From ELFIN Measurements and Statistical Lifetime Models

We investigate three different periods in the aftermath of different geomagnetic storms and substorms. The first period took place on September 5–7, 2020 and corresponds to moderate geomagnetic activity with $Dst > -21$ nT, $\langle Kp \rangle \simeq 1$, and 1-min SuperMAG auroral electrojet index SME ∈ [100 − 300] nT (Gjerloev, 2012; Newell & Gjerloev, 2011). Five days earlier, on August 31, a geomagnetic storm had reached a

minimum $Dst = -59$ nT, with strong substorms ($Kp \simeq 2-4$, SME $\simeq 500-800$ nT) until 12:30 UT on September 5. Such geomagnetic storm and strong substorms are usually accompanied by important injections of 100–500 keV electrons deep into the radiation belts (Turner et al., 2015, 2017). In addition, lower energy anisotropic electrons and ions injected during substorms can locally generate chorus waves outside the eroded plasmasphere, hiss waves inside the plasmasphere, and EMIC waves down to $L^* \sim 3.5$ (Artemyev et al., 2016; Chen et al., 2010; Kennel & Petschek, 1966; Li et al., 2010; Liu et al., 2020; Tsurutani & Smith, 1977). Such waves, alone or in combination, can subsequently precipitate relativistic electrons into the atmosphere (Artemyev et al., 2016; Kersten et al., 2014; Li et al., 2015; Meredith et al., 2009; Mourenas et al., 2016, 2017; Ni et al., 2015; Pinto et al., 2019; Simms et al., 2018; Su et al., 2016).

Therefore, it is interesting to examine the evolution of electron fluxes in the outer radiation belt during the period starting at 13 UT on September 5. Over $L^* \simeq 3.5$–6.6, the trapped 0.1–1 MeV electron flux measured just above α_{LC} by ELFIN shows a clear MLT periodicity, with higher fluxes recorded at 0–1 MLT, corresponding to fixed longitudes far from the SAA (see Section 2.1). Accordingly, we calculate lifetimes τ_L based on the assumed exponential decay of the trapped electron flux measured at 0–1 MLT by ELFIN-A at 13:05 UT on September 5 and at 13:30 UT on September 7. During this period, $L_{pp} \sim 4.75$ at 0–1 MLT based on statistical plasmapause models parameterized by *Dst* and *Kp* (O'Brien & Moldwin, 2003).

Inside the plasmasphere at $L^* < L_{pp} \sim 4.75$, Figures 3a and 3b show a reasonable agreement from 70 keV up to ~5 MeV between electron lifetimes τ_L directly obtained from ELFIN measurements and the statistical model of theoretical electron lifetimes (Mourenas et al., 2017) based on electron quasilinear diffusion by typical plasmaspheric hiss and EMIC waves, taking a plasmasphere density equal ($\eta = 1$) to its statistical average level (Ozhogin et al., 2012). In particular, contours of constant measured lifetimes (in black) correspond to higher energies at lower L^* as expected from the statistical model of theoretical lifetimes (in yellow). The increase of measured lifetimes from 1 day to 6 days as electron energy increases between ~0.2 and 1 MeV follows theoretical expectation for hiss-driven electron loss (Mourenas et al., 2017). At higher energy, there is a noticeable decrease of measured electron lifetimes to less than 6 days near 3–4 MeV at $L^* \sim 4.5$, which roughly corresponds to the expected domain of lifetime reduction by combined effects of hiss and hydrogen band EMIC waves (Mourenas et al., 2016, 2017).

It is worth emphasizing that the measured electron lifetimes displayed in Figure 3 are inferred from electron flux decay observed by ELFIN over only a very short two-day period. Consequently, measured electron lifetimes longer than ~4 days cannot be determined as accurately as shorter lifetimes. This may explain some local deviations of measured lifetimes by a factor ~2 from theoretical lifetimes. In addition, the present theoretical lifetimes are based on statistical models of hiss and EMIC waves derived from years of satellite data. During a given two-day period, the actual MLT-averaged wave power and frequency of hiss and EMIC waves on a given L^*-shell can obviously vary from their time-averaged values for a given *Kp* or AE. Notwithstanding, measured and theoretical lifetimes quantitatively agree below 500 keV in Figure 3b, and their general trends as a function of electron energy and L^* remain similar up to 5 MeV inside the plasmasphere, demonstrating the reliability of statistical wave and lifetime models over periods of several days or more (Agapitov et al., 2020).

Above the plasmapause (from $L^* = 4.75 \sim L_{pp}$ up to $L^* = 6.6$), Figures 3a and 3c similarly show a good agreement between electron lifetimes directly measured by ELFIN and the statistical model of electron lifetimes based on electron quasi-linear diffusion by chorus and hydrogen-band EMIC waves (Mourenas et al., 2016, 2017; Zhang et al., 2017). One can notice the presence of two minimas in measured electron lifetimes, near 100 keV and 2–3 MeV, in agreement with statistical models of lifetimes corresponding to electron scattering by chorus waves in the plasma trough, and by EMIC waves in a plasmaspheric plume (with $\eta = 1$ here), at different MLTs. There is a clear and strong effect of EMIC wave-driven electron pitch-angle scattering which, combined with chorus-driven scattering, produces the second deep minimum of electron lifetimes $\tau_L \sim 2$ days near 2–3 MeV, as theoretically expected (Mourenas et al., 2016). Weak EMIC-like signals up to half the proton gyrofrequency were recorded on the duskside during this period at Gillam CARISMA ground station near $L^* = 6$.

The second investigated period extends from November 7 (22:45 UT) to November 9 (23:00 UT), corresponding to $\langle Kp \rangle \sim 1$ and SME $\sim 100-300$ nT. This period immediately follows a peak of substorm activity

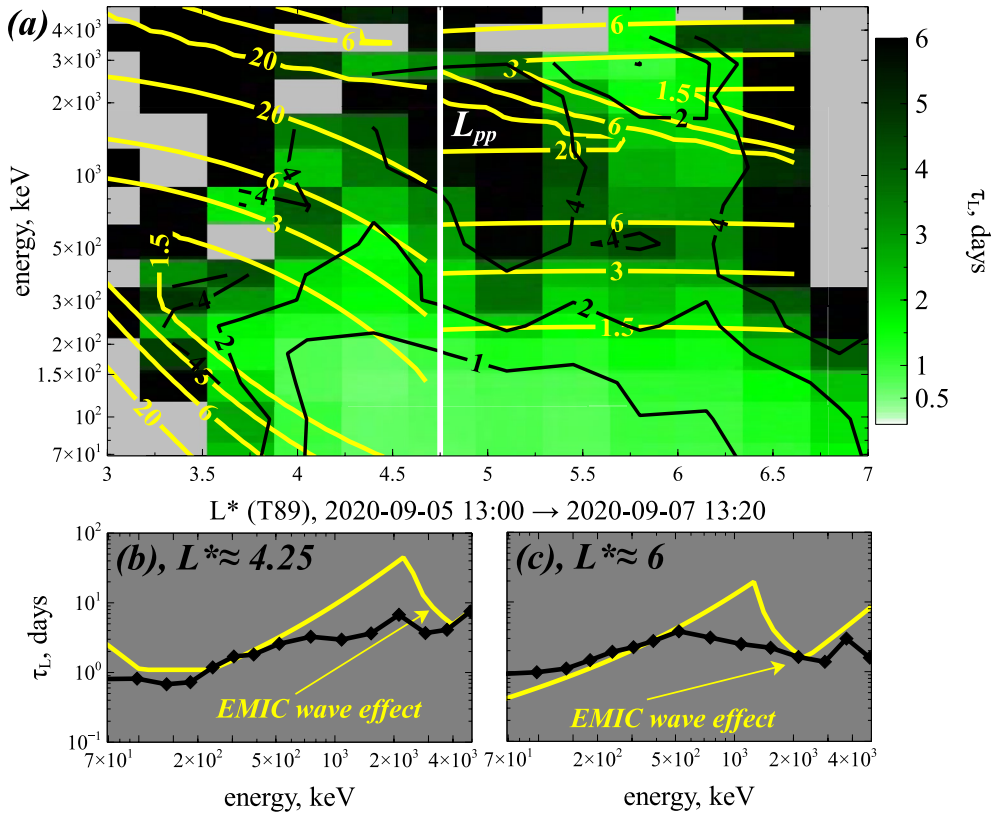

Figure 3. (a) Map of electron lifetimes τ_L as a function of L^* and electron energy between 13 UT on September 5, 2020 and 13:20 UT on September 7. Lifetimes directly calculated from the observed decay of trapped electron fluxes measured by Electron Loss and Fields Investigation (ELFIN)-A at 1 MLT during this period (color bins and black contour lines) are compared with statistical models of theoretical electron lifetimes (yellow contour lines), resulting from combined hiss and hydrogen-band electromagnetic ion cyclotron (EMIC) wave driven pitch-angle scattering at $L^* < L_{pp} \sim 4.75$ inside the plasmasphere (Mourenas et al., 2017) (using $\langle Kp \rangle = 1$ and a plasma density level $\eta = 1$ given by Ozhogin et al. (2012)) and from combined chorus and hydrogen-band EMIC wave driven scattering at $L^* > L_{pp}$, where EMIC waves are assumed present in a plume (Aryan et al., 2020; Mourenas et al., 2017; Zhang et al., 2017). Gray color shows bins without reliable ELFIN measurements (insufficiently high counts). (b, c) Profiles of τ_L versus electron energy derived from ELFIN-A measurements (black) and obtained from the statistical model of electron lifetimes (yellow) for two L^*-shells. The decrease of τ_L (as compared with hiss or chorus wave-driven electron loss alone) caused by EMIC wave-driven scattering is indicated by a yellow arrow.

reaching $Kp = 3$ and SME $\sim$ 400 nT at 21:00–22:30 UT on November 7. Six days earlier, there was also a moderate geomagnetic storm with a minimum $Dst = -35$ nT. Figures 4a and 4c show that measured electron lifetimes (calculated between maximas of ELFIN's trapped flux near 9 MLT) are in rough agreement with the statistical model of electron lifetimes for chorus and EMIC wave-driven loss (considering a typical duskside plasmaspheric plume density, with $\eta = 1$) when 100 < AE(nT)< 300 (Aryan et al., 2020; Mourenas et al., 2016, 2017) over $L_{pp}(Kp) \sim 4.3 < L^* < 6$. In particular, one notices again the presence of two minimas of lifetimes, near 100 keV and 1–2 MeV, as expected from statistical lifetimes models.

However, the observed minimum lifetimes $\tau_L \sim 1$ day occur here at a slightly lower energy ($\sim 1-2$ MeV) than during the first investigated period, probably due to a larger plasma density in the duskside MLT sector where EMIC waves were likely present than in the statistical model from Ozhogin et al. (2012) and/or to a higher upper cutoff frequency of hydrogen-band EMIC waves (Mourenas et al., 2016; Summers & Thorne, 2003) during this particular period than in statistical models (Kersten et al., 2014; Zhang et al., 2016). Accordingly, Figures 4b and 4d show electron lifetimes from the statistical model calculated for a 60% higher plasma density (that is, $\eta = 1.6$) in the duskside plasmaspheric plume where EMIC waves are assumed to be present, indeed demonstrating a much better agreement with measured lifetimes at high energies. Similar theoretical lifetimes could be obtained using the same plasmaspheric plume density ($\eta = 1$)

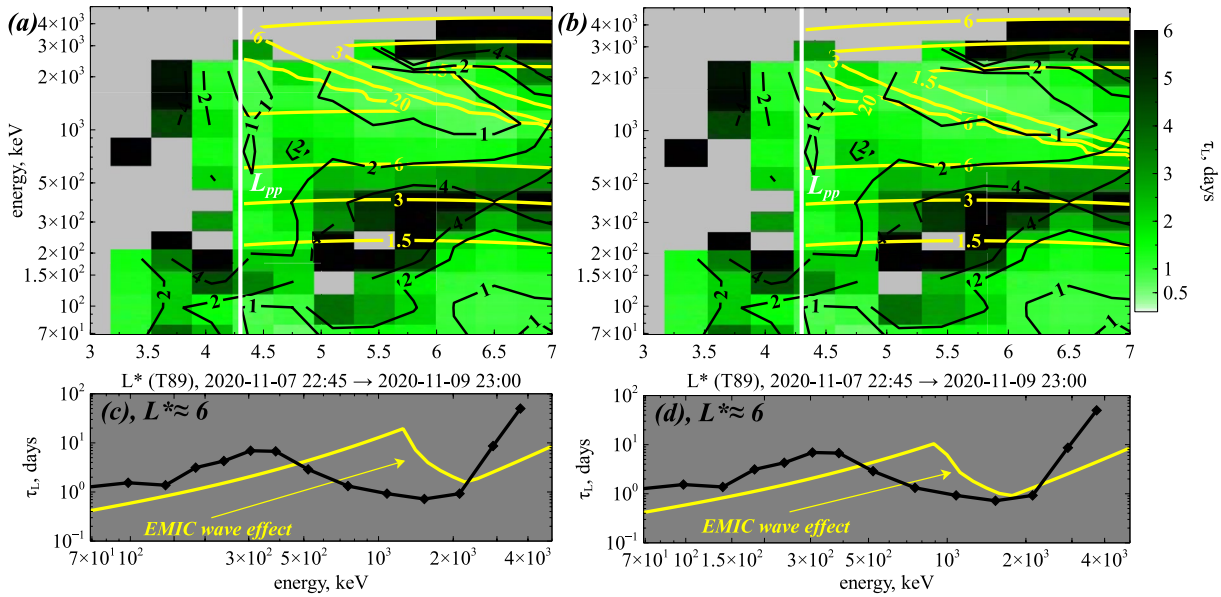

Figure 4. (a) Map of electron lifetimes τ_L as a function of L^* and electron energy between 22:45 UT on November 7, 2020 and 23:00 UT on November 9, 2020. Lifetimes directly calculated from the observed decay of trapped electron fluxes measured by Electron Loss and Fields Investigation (ELFIN)-B at 9 MLT during this period (color bins and black contour lines) are compared with a statistical model of electron lifetimes (yellow contour lines) resulting from combined lower-band chorus and hydrogen-band EMIC wave scattering outside the plasmasphere from $L^* \sim L_{pp} \sim 4.3$ to $L^* = 6.6$, using $\eta = 1$ for a typical duskside plasmaspheric plume density (Aryan et al., 2020; Mourenas et al., 2016, 2017). (b) Same as (a) but with lifetimes from the statistical model calculated using $\eta = 1.6$, that is, for a 60% higher plasma density in the duskside plasmaspheric plume where EMIC waves are assumed to be present. Gray color shows bins without reliable ELFIN measurements (insufficiently high counts). (c) Profiles of τ_L versus electron energy derived from ELFIN-B measurements (black) and obtained from the statistical model of electron lifetimes (yellow) from panel (a) at $L^* = 6$. (d) Same as (c) but with the model of electron lifetimes from panel (b). The decrease of τ_L (as compared with chorus wave-driven loss alone) due to EMIC wave-driven scattering is indicated by a yellow arrow.

as in Figures 4a and 4c but with a higher upper cutoff frequency of EMIC waves near 0.53 times the proton gyrofrequency. Weak EMIC-like signals up to half the proton gyrofrequency were recorded on the duskside during this period at Gillam CARISMA ground station near $L^* = 6$.

The third selected period extends from 09:10 UT on November 28 to 08:20 UT on December 4, 2020. This 6-day period follows a moderate geomagnetic storm reaching $Dst \sim -40$ nT on November 22 (with maximum $Kp = 4.7$ and maximum SME = 1200 nT), with a long recovery phase comprising many substorms with SME $\sim 400 - 500$ nT on November 23, 25, and 27. Disturbances remained moderate during the selected period (SME $\in$ [100, 300] nT, $\langle Kp \rangle \sim 1$, $Dst > -19$ nT), with a minimum plasmapause position $L_{pp}(Kp, Dst) \simeq 4.0$ near 10 MLT (O'Brien & Moldwin, 2003).

In Figures 5a and 5c, lifetimes inferred from the exponential decay of trapped electron fluxes measured by ELFIN-A outside the plasmasphere near 10 MLT (where high maximas of trapped $0.1 - 1$ MeV electron fluxes are observed) agree well from $\sim$ 100 keV to 2 MeV with statistical electron lifetimes due to chorus wave scattering alone (Aryan et al., 2020) during moderate activity ($100 < \text{AE(nT)} < 300$). The absence of a second lifetime minimum at ~2 MeV is probably due to the absence of a plasmaspheric plume containing hydrogen-band EMIC waves during this particular period. Plasma density at $L^* > 4$ outside the plasmasphere (Sheeley et al., 2001) is indeed less than 20% of the statistical plasmaspheric density (Ozhogin et al., 2012), giving a minimum electron energy of cyclotron resonance with hydrogen-band EMIC waves larger than 3.5 MeV for a typical upper cutoff frequency ~0.45 times the proton gyrofrequency (Mourenas et al., 2016; Zhang et al., 2016). Inside the plasmasphere, statistical electron lifetimes corresponding to hiss-driven loss (Mourenas et al., 2017) are in rough agreement with measured lifetimes at $L^* < L_{pp}$ in Figures 5a and 5b, except for a narrow zone of longer lifetimes close to the plasmapause where hiss wave power is often weak (Malaspina et al., 2016).

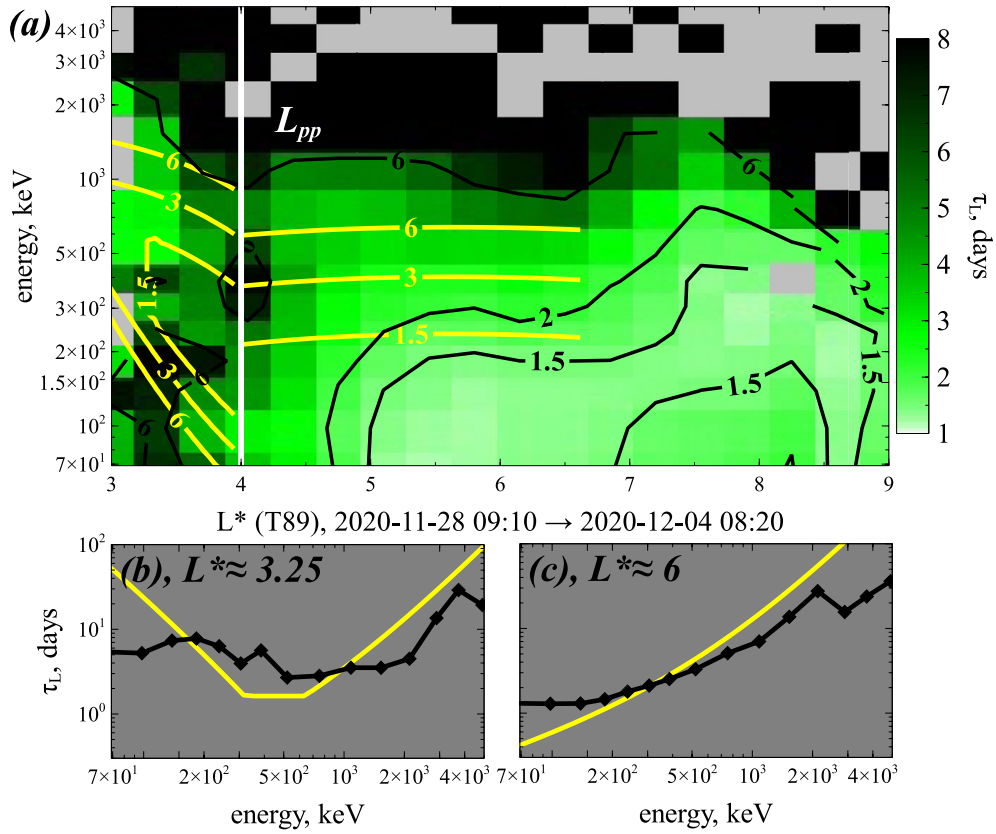

Figure 5. (a) Map of electron lifetimes τ_L as a function of L^* and electron energy between 09:10 UT on November 28, 2020 and 08:20 UT on December 4, 2020. Lifetimes directly calculated from the observed decay of trapped electron fluxes measured by Electron Loss and Fields Investigation (ELFIN)-A near 10 MLT during this period (color bins and black contour lines) are compared with statistical models of electron lifetimes (yellow contour lines) resulting from lower-band chorus wave scattering alone (using $R_{EMIC} = 1$) outside the plasmasphere from $L^* \sim L_{pp} \sim 4.0$ to $L^* = 6.6$ (Aryan et al., 2020), and resulting from hiss wave-driven loss (for $\langle Kp \rangle = 1$) inside the plasmasphere (Mourenas et al., 2017). Gray color shows bins without reliable ELFIN measurements (insufficiently high counts). (b and c) Profiles of τ_L versus electron energy derived from ELFIN measurements (black) and obtained from the statistical model of electron lifetimes (yellow) for two L^*-shells.

3. Diffusion Rates Inferred From Precipitated and Trapped Electron Fluxes Measured by ELFIN

3.1. Generalities

Based on quasilinear diffusion theory (Kennel & Petschek, 1966; Li et al., 2013) in the presence of mainly moderate amplitude (< 150pT) short chorus wave packets (Tao et al., 2012; Zhang et al., 2019; Zhang, Agapitov, et al., 2020), the precipitated to trapped electron flux ratio $J_{precip}/J_{trapped}$ can be expressed as a function of the pitch-angle diffusion rate $D_{\alpha\alpha,LC}$ of electrons by whistler-mode chorus waves at the loss cone angle. Equatorial loss cone angles are $\alpha_{LC} \simeq 3.75°$ for $L^* = 5$ and $\alpha_{LC} \simeq 2.8°$ for $L^* = 6$, and corresponding bounce periods τ_B of 100 keV electrons at the loss cone angle are $\tau_B \simeq 1.0$ s and $\tau_B \simeq 1.15$ s, respectively, in a near quiet T89 geomagnetic field (Schulz & Lanzerotti, 1974; Zhou et al., 2013).

Let us define $z_0 = \alpha_{LC}/\sqrt{D_{\alpha\alpha,LC}\cos\alpha_{LC}\tau_B/4} \simeq 2\alpha_{LC}/\sqrt{D_{\alpha\alpha,LC}\tau_B}$ for $4 \le L^* \le 6$, with $D_{\alpha\alpha,LC}$ in s^{-1} and equatorial pitch-angles α in rad. For realistic values of $D_{\alpha\alpha,LC} < 4.2 \times 10^{-4}$ s^{-1} and $C = |\delta\alpha|/\alpha_{LC} = |\alpha_{precip}/\alpha_{LC} - 1| \le 0.73$, we get $z_0 > 4.5$ and $(1 - C)z_0 > 1.2$. In this case, we can safely keep only the first term of series expansions of modified Bessel functions $I_0([1 - C]z_0)$ and $I_1(z_0)$ for large arguments (Abramowitz & Stegun, 1972), and the flux ratio (Kennel & Petschek, 1966; Li et al., 2013) can be rewritten under the form

$$\frac{J_{trapped}}{J_{precip}} = A \simeq (1 + z_0\, B)(1 - C)^{1/2}\exp(z_0\, C) \tag{5}$$

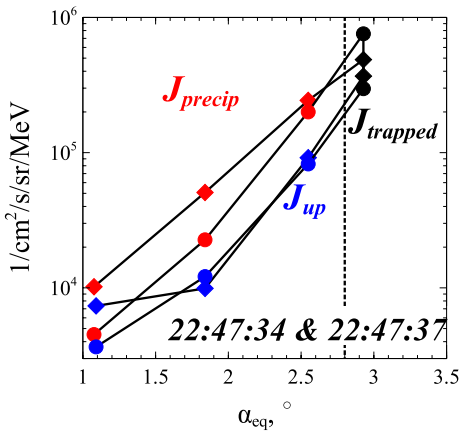

Figure 6. Equatorial pitch-angle distributions of 100 ± 30 keV electron flux at $L^* \simeq 6$ and 22:47 UT (at 9 MLT and 240° magnetic longitude) on November 7, 2020, measured during two successive spin periods (3 s) of Electron Loss and Fields Investigation (ELFIN)-B. Precipitated (J_{precip}), trapped ($J_{trapped}$), and upward backscattered fluxes (J_{up}) are shown by red, black, and blue symbols, respectively. Measurements during the first and second spin periods are shown by circles and diamonds, respectively. The vertical dotted line shows the loss cone angle.

with $B = \ln(\sin\alpha_{trapped}/\sin\alpha_{LC})$. The exact solution to Equation 5 is simply:

$$z_0 = \frac{1}{C} W\left(\frac{A\,C\exp(C/B)}{B\sqrt{1-C}}\right) - \frac{1}{B} \quad (6)$$

with W the product logarithm function, also called Lambert-W function (Abramowitz & Stegun, 1972; Fukushima, 2013). For a fixed value of $\alpha_{trapped}/\alpha_{LC} \geq 1$, the inferred $D_{\alpha\alpha,LC} = (2\alpha_{LC}/z_0)^2/\tau_B$ varies approximately like $\sim (\ln(J_{precip}/J_{trapped})\,\delta\alpha)^2$. The relative error of the analytical solution Equation 6 compared to the numerical solution of the exact equation (Kennel & Petschek, 1966) remains smaller than 15% when $J_{precip}/J_{trapped} < 0.3$ for $B < 0.06$ and $C \leq 0.73$ at $L^* \leq 6$, that is, not too close to the strong diffusion regime (Schulz & Lanzerotti, 1974; Zhou et al., 2013).

It is worth emphasizing that chorus wave driven diffusion rates $D_{\alpha\alpha,LC}$ at $L^* = 4.5$–6.5 decrease rapidly as electron energy increases above 10 keV for fixed wave power and plasma density (Aryan et al., 2020; Mourenas et al., 2014), and that a larger $D_{\alpha\alpha,LC}$ is likely to be more accurately estimated from the measured flux ratio $J_{precip}/J_{trapped}$ (Reidy et al., 2021). This leads us to focus on measured fluxes of 100 ± 30 keV electrons, slightly above the minimum energy limit of ELFIN's detector (Angelopoulos et al., 2020).

3.2. Taking Atmospheric Backscatter Into Account

Numerical simulations show that ~80 − 90% of the ~100 − 200 keV precipitated electrons with initial pitch angles very close to α_{LC} (as well as a fraction of electrons initially just above α_{LC}) should be backscattered by collisions in the atmosphere with a final $\alpha \sim (0.0\text{–}0.95) \times \alpha_{LC}$, while ≈ 25 − 70% of the precipitated electrons deeper inside the loss cone should be backscattered with roughly similar pitch-angles, with a final energy of backscattered electrons ≈ 60 − 95% of their initial energy (Marshall & Bortnik, 2018; Selesnick et al., 2004). A detailed analysis of backscattered electron fluxes measured by ELFIN is beyond the scope of the present study. However, it is important to examine here whether backscattered electrons from the conjugate region contribute significantly to the precipitated electron flux measured by ELFIN, since this may represent a complication for accurately inferring wave-driven diffusion rates.

Assuming a system nearly symmetric about the magnetic equator at $L^* = 5$–6 over timescales $\Delta t \gg \tau_B \sim 1$ s, the backscattered upward electron flux J_{up} detected inside the loss cone below ELFIN (e.g., see Figure 6) should provide a good estimate of the backscattered electron flux $J_{down,bs}$ coming from the conjugate region (on the same geomagnetic field line) and precipitated below ELFIN. Taking into account the smooth transition between trapped and loss cone particle distributions in numerical simulations (Marshall & Bortnik, 2018), the very slight difference, in the investigated cases, between North and South α_{LC} values is neglected. We also neglect the impact on the backscattered loss cone electron distribution of additional nonlinear resonant interactions with intense chorus waves, which could efficiently send electrons outside the loss cone via anomalous trapping (Artemyev et al., 2021; Gan et al., 2020; Kitahara & Katoh, 2019). In the presence of a typical distribution of mostly short and low to moderate amplitude chorus wave packets (Mourenas et al., 2018; Zhang et al., 2018, 2019), test particle simulations (see Appendix A) indeed show that nonlinear wave-particle interactions should not decrease the number of backscattered loss cone electrons during their rapid journey from the conjugate region to ELFIN, because anomalous trapping effects are strongly reduced for short or low amplitude wave packets. Therefore, the backscattered electron flux from the conjugate region $J_{down,bs} \simeq J_{up}$ must be subtracted from the total precipitated flux J_{precip} measured by ELFIN (see Figure 6) to estimate the actual flux of electrons directly sent into the loss cone by wave-driven pitch-angle diffusion. This precipitated flux corrected for backscatter, $J^{corr}_{precip} = J_{precip} - J_{down,bs} \simeq J_{precip} - J_{up}$, can be used in Equations 5 and 6 to obtain a more accurate estimate of $D_{\alpha\alpha,LC}$.

Such diffusion rates $D_{\alpha\alpha,LC}$ inferred from ELFIN electron flux measurements are compared below with time-averaged theoretical diffusion rates based on comprehensive statistics of chorus waves (Agapitov

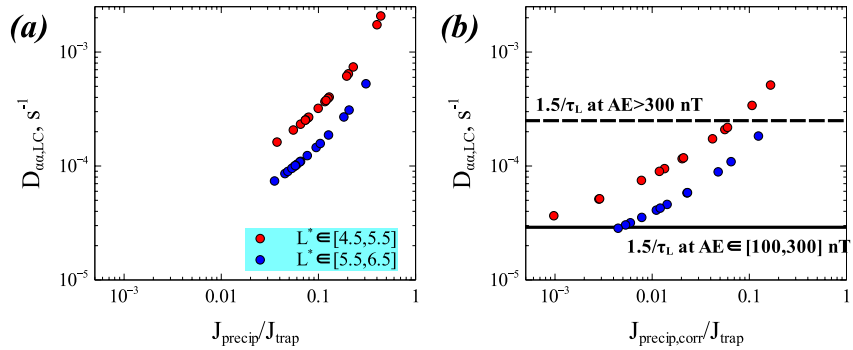

Figure 7. (a) Quasilinear pitch-angle diffusion rates $D_{\alpha\alpha,LC}$ of 100 ± 30 keV electrons by lower-band chorus waves, inferred using Equation 6 from the ratio $J_{precip}/J_{trapped}$ of precipitated 100 ± 30 keV electron flux (at $\delta\alpha/\alpha_{LC} = -0.27$) over trapped electron flux (at $\delta\alpha/\alpha_{LC} = +0.05$) measured by Electron Loss and Fields Investigation (ELFIN) in the dawn sector, at various moments during periods of generally moderate geomagnetic activity (100 < AE ≈ SME(nT) < 300), at $L^* = 5$ (red points) and $L^* = 6$ (blue points). (b) Same as (a) but using now the ratio $J^{corr}_{precip}/J_{trapped}$ of measured precipitated electron flux *corrected for atmospheric backscatter*, over measured trapped flux. Horizontal black solid and dashed lines indicate dawn sector statistical diffusion rates $\langle D_{\alpha\alpha,LC}\rangle \sim 1.5/\tau_L$ at $L^* = 5$–6 based on chorus wave statistics for 100 < *AE* ≈ *SME*(nT)< 300 and for *AE* > 300 nT, respectively.

et al., 2018, 2019; Aryan et al., 2020). The theoretical MLT-averaged and time-averaged quasi-linear pitch-angle diffusion rate of 100 keV electrons by lower-band chorus waves at $L^* = 5$–6 is approximately given by $\langle D_{\alpha\alpha,LC}\rangle \simeq 1/\tau_L$ (Albert & Shprits, 2009; Artemyev et al., 2013; Mourenas et al., 2014), with τ_L the statistical lifetime of 100 keV electrons (Aryan et al., 2020). But since the presently analyzed ELFIN measurements were performed in the dawn sector, where chorus wave power is ≈ 3 times stronger than on the duskside (Agapitov et al., 2018, 2019; Aryan et al., 2020), diffusion rates inferred from ELFIN electron flux measurements must be compared with the slightly larger dawn sector statistical diffusion rate, $\langle D_{\alpha\alpha,LC}\rangle \sim 1.5/\tau_L$, with τ_L given by Equations 1 and 4 for 100 < *AE* ≈ *SME*(nT)< 300 and by Aryan et al. (2020) for AE ≈ SME > 300 nT.

3.3. Comparisons Between Diffusion Rates Inferred From ELFIN Measurements and Statistical Diffusion Rates

Figure 7a shows electron pitch-angle diffusion rates $D_{\alpha\alpha,LC}$ inferred by directly substituting in Equation 6 the ratio $J_{precip}/J_{trapped}$ of precipitated (at $\delta\alpha/\alpha_{LC} = -0.27$) to trapped (at $\delta\alpha/\alpha_{LC} = +0.05$) fluxes of 100 ± 30 keV electrons measured by ELFIN (during 10–60 s, that is, averaged over ∼ 3 to 20 spin periods). ELFIN measurements are performed near 9–10 MLT, at various moments randomly distributed during the two periods in November to early December 2020 already discussed in Section 2. Such periods correspond to a moderate average level of geomagnetic activity with $\langle Kp\rangle \simeq 1$ and mostly 100 < SME(nT)< 300, including short bursts of substorm activity reaching SME ∼ 300 − 450 nT (but max(*Kp*) < 3.3). Figure 7a shows that keeping in Equation 6 the total precipitated electron flux J_{precip} measured by ELFIN gives very large diffusion rates $D_{\alpha\alpha,LC} \sim 10^{-4}$–$2 \times 10^{-3}$ s^{-1}. This is much larger than the expected statistical average level $\langle D_{\alpha\alpha,LC}\rangle \simeq 1.5/\tau_L \simeq 3 \times 10^{-5}$ s^{-1} during such mostly moderate disturbances with 100 < AE ≈ SME(nT)< 300. Nearly 50% of the inferred $D_{\alpha\alpha,LC}$ values are even higher than the statistical average level $\langle D_{\alpha\alpha,LC}\rangle \simeq 2.5 \times 10^{-4}$ s^{-1} expected during strong disturbances with AE ≈ SME > 300 nT. This discrepancy contrasts with the good agreement found in Section 2 between lifetimes obtained from electron flux decay measured by ELFIN during the same periods and lifetimes from the same statistical model for 100 < AE(nT)< 300. Such an inconsistency suggests that the inferred diffusion rates in Figure 7a are likely overestimated.

Accordingly, we use in Figure 7b the precipitated 100 ± 30 keV electron flux corrected for atmospheric backscatter, $J^{corr}_{precip} = J_{precip} - J_{down,bs} \simeq J_{precip} - J_{up}$, in Equation 6 to get better estimates of $D_{\alpha\alpha,LC}$. The upward backscattered to precipitated electron flux ratio J_{up}/J_{precip} measured by ELFIN at $L^* = 5$–6 has a mean value ≃0.8 at $\delta\alpha/\alpha_{LC} = -0.27$ during the considered events, suggesting an important effect of this correction. Figure 7b shows that diffusion rates inferred from the corrected ratio $J^{corr}_{precip}/J_{trapped}$ are indeed significantly reduced as compared with Figure 7a. Now, most values are in the range $D_{\alpha\alpha,LC} \simeq 2.8 \times 10^{-5}$–$10^{-4}$ s^{-1}, in

Table 1
Variation of Inferred $D_{\alpha\alpha,LC}$ (s^{-1}) With SME (nT) in Figure 7b

$D_{\alpha\alpha,LC}$	$D_{\alpha\alpha,LC}$	⟨SME⟩	max(SME)
Range	Mean	Mean (median)	Mean (median)
$(2.8-5)\times10^{-5}$	3.7×10^{-5}	121 (107)	199 (177)
$(0.5-1)\times10^{-4}$	7.1×10^{-5}	142 (125)	322 (328)
$(1.0-5)\times10^{-4}$	2.2×10^{-4}	163 (150)	312 (272)

reasonable agreement with the statistical estimate $\sim 1.5/\tau_L$ in the dawn sector when 100 < AE(nT)< 300. The agreement is better at $L^* \simeq 6$ (blue points) than at $L^* \simeq 5$ (red points), probably due to a slightly stronger chorus wave power at $L^* = 5$ near 9–10 MLT during these periods than in time-averaged statistics.

The magnitude of chorus wave-driven diffusion rates $D_{\alpha\alpha,LC}$ is known to statistically increase with geomagnetic activity (Agapitov et al., 2018, 2019; Aryan et al., 2020; Meredith et al., 2001). Therefore, it is important to check whether the inferred diffusion rates in Figure 7b show a similar dependence on geomagnetic activity. To perform a rough statistical study based on our limited data set of 25 points in Figure 7b, we separate these inferred $D_{\alpha\alpha,LC}$ in three different groups of 8–9 points, corresponding to three different ranges of $D_{\alpha\alpha,LC}$ values.

Table 1 provides the mean value of the inferred $D_{\alpha\alpha,LC}$ in each of these three different groups, together with the corresponding mean (and median) value of the average SME index, denoted ⟨SME⟩, during the two hours preceding ELFIN measurements, and the mean (and median) value of the maximum 1-min SME, denoted max(SME), during the two hours preceding ELFIN measurements. It shows that, on average, the smallest inferred $D_{\alpha\alpha,LC}$ values correspond to the smallest ⟨SME⟩ ∼ 121 nT and max(SME) ∼ 199 nT. This is consistent with the good agreement obtained in Figure 7b between the 8 smallest inferred $D_{\alpha\alpha,LC}$ values and the expected statistical diffusion rate for 100 < AE(nT)< 300. The largest inferred values $D_{\alpha\alpha,LC} > 5\times10^{-5}$ s^{-1} are generally obtained after 2-hr periods comprising strong bursts of auroral activity reaching max(SME) > 270–300 nT. Such substorms are usually associated with significant injections of 5–30 keV electrons from the plasma sheet that generate stronger chorus waves, leading to larger $D_{\alpha\alpha,LC}$ values (Boyd et al., 2014; Li et al., 2010; Meredith et al., 2001; Omura et al., 2008; Zhang et al., 2019). The results displayed in Figure 7b and Table 1 therefore demonstrate that the diffusion rates $D_{\alpha\alpha,LC}$, inferred from the ratio of precipitated (corrected for backscatter) to trapped electron fluxes measured by ELFIN, are in reasonable agreement with statistical models of electron quasi-linear diffusion by chorus waves, parameterized by geomagnetic activity (Agapitov et al., 2018; Aryan et al., 2020).

3.4. Two Detailed Case Studies

Let us examine in more detail the equatorial pitch-angle distribution of 100 keV electron fluxes measured by ELFIN-A near 10 MLT and $L^* = 6$, at two different times in November 2020. These two selected cases are representative of typical observations.

Figure 8a shows that at 9:10 UT on November 28, the precipitated 100 ± 30 keV electron flux J_{precip} first steeply decreases by a factor ∼20 between $\alpha_{LC} \simeq 2.8°$ and $\alpha = 1.75°$, before decreasing much more slowly (by a factor ∼2.5) between $\alpha = 1.75°$ and $\alpha = 0.75°$. This behavior is at odds with predictions from quasi-linear theory (Kennel & Petschek, 1966; Li et al., 2013). Instead, it is reminiscent of the typical shape of pitch-angle distributions produced by atmospheric backscatter (Marshall & Bortnik, 2018). This is confirmed by simultaneous ELFIN-A measurements of the upward backscattered electron flux J_{up}, since J_{up} is only ∼20% smaller than J_{precip} at all $\alpha < 0.95\alpha_{LC}$ in Figure 8a, like in most pitch-angle distributions measured during moderate disturbances. Actually, in a system symmetric about the equator, atmospheric backscatter in the two conjugate regions should produce very similar downward and upward backscattered electron fluxes, $J_{\text{down,bs}} = J_{\text{up}}$, at ELFIN-A's position. Therefore, the observed slower decrease of the precipitated flux deeper inside the loss cone is consistent with a minimum level imposed by atmospheric backscatter from the conjugate region.

Figure 8b shows that the precipitated electron flux corrected for backscatter, $J^{corr}_{precip} = J_{precip} - J_{up}$, decreases faster than J_{precip} inside the loss cone. The theoretical fit (dashed blue line) to the pitch-angle distribution shape, given by Equation 5, is roughly consistent with the measured distribution (at least down to $\alpha \simeq 1.6°$). This corresponds to a moderate inferred pitch-angle diffusion rate $D_{\alpha\alpha,LC} \simeq 3.5\times10^{-5}$ s^{-1}, in good agreement with the expected statistical level $\langle D_{\alpha\alpha,LC}\rangle \simeq 1.5/\tau_L \simeq 3\times10^{-5}$ s^{-1} for AE ∈ [100, 300] nT, since the 1-min

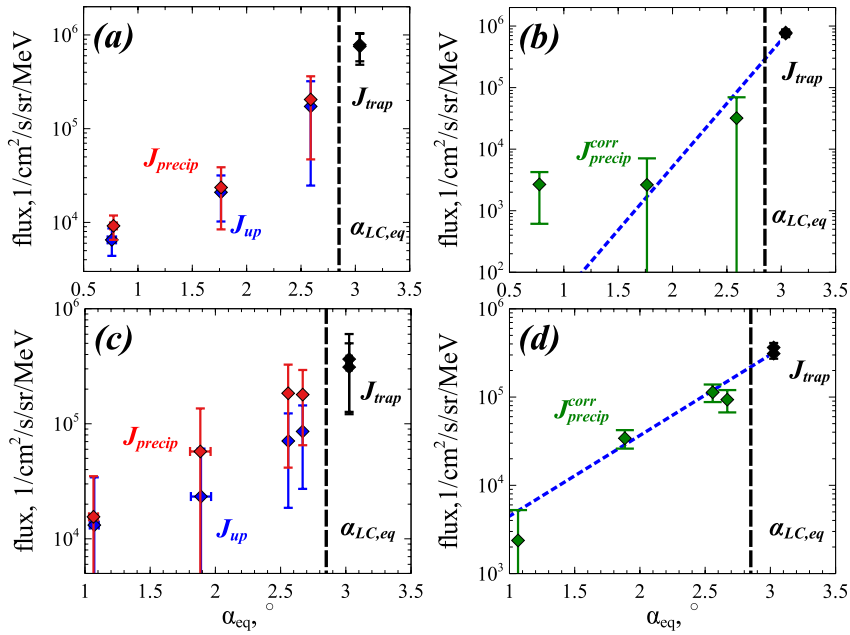

Figure 8. (a) Equatorial pitch-angle distribution of 100 ± 30 keV electron flux measured by Electron Loss and Fields Investigation (ELFIN)-A at 9:10 UT (10 MLT) on November 28, 2020 at $L^* = 6$, including precipitated (J_{precip}), trapped ($J_{trapped}$), and upward backscattered fluxes (J_{up}). Diamonds show time-averaged electron fluxes measured over ∼30–60 s. Vertical bars show the maximum and minimum 3-s flux values recorded during two different spin periods of ELFIN within this time interval. Electron fluxes higher than 10^4 e/cm²/sr/s/MeV are measured with a signal-to-noise ratio better than 50:1. (b) Same as (a) but showing the time-averaged precipitated electron flux corrected for atmospheric backscatter $J^{corr}_{precip} = J_{precip} - J_{up}$ and the trapped flux. Error bars are calculated as the sum of standard errors $\sigma/\sqrt{n}$ of the mean J_{precip} and J_{up} values, with σ the standard deviation and $n \simeq 12$–20 the number of 3-s flux data points (or spin periods) used at each pitch-angle (relative standard errors of mean fluxes are ≃10%). (c, d) Same as (a, b) at 22:45 UT (9 MLT) on November 7, 2020. The theoretical shape from Equation 5 of the pitch-angle distribution near and within the loss cone is shown in panels (b, d) by a dashed blue line (fitted to the three points of highest $J_{trapped}$ and J_{precip}, expected to be more reliable).

SME index varied between 75 and 183 nT, with an average value of 100 nT, during the two hours preceding ELFIN-A measurements at 9:10 UT.

The pitch-angle electron distribution measured by ELFIN-B at 22:45 UT on November 7 is displayed in Figure 8c. The precipitated 100 ± 30 keV electron flux J_{precip} decreases less steeply inside the loss cone in Figure 8c as compared with Figure 8a, and the upward backscattered electron flux J_{up} inside the loss cone is now ∼2 − 3 times smaller than J_{precip}. However, the ratio $J_{up}(\alpha)/J_{trapped}(1.05\alpha_{LC})$ is very similar in Figures 8c and 8a for $\alpha/\alpha_{LC} \simeq 0.70$–0.95, consistent with atmospheric backscatter (Marshall & Bortnik, 2018).

Figure 8d shows that the precipitated electron flux corrected for backscatter, $J^{corr}_{precip} = J_{precip} - J_{up}$, decreases only slightly faster than J_{precip} inside the loss cone. This corresponds to a large inferred pitch-angle diffusion rate $D_{\alpha\alpha,LC} \simeq 1.9 \times 10^{-4}$ s^{-1}, much larger than in the previous case. The average value of SME during the two hours preceding ELFIN measurements was ≃260 nT, with a maximum of 633 nT. Such average and maximum SME values are much larger than for the 28 November (9:10 UT) case, and likely correspond to the presence of much more intense chorus waves (Agapitov et al., 2019; Aryan et al., 2020; Li et al., 2011; Meredith et al., 2001). The expected statistical level $\langle D_{\alpha\alpha,LC}\rangle \simeq 1.5/\tau_L \simeq 2.5 \times 10^{-4}$ s^{-1} for AE > 300 nT is consistent with the inferred $D_{\alpha\alpha,LC}$. In addition, there is a good agreement in Figure 8d between the theoretical shape of the pitch-angle distribution given by Equation 5 and the actual pitch-angle distribution measured by ELFIN-B.

Finally, it is instructive to check whether instantaneous diffusion rates $D_{\alpha\alpha,LC}$, inferred from the precipitated to trapped electron flux ratio measured by ELFIN, vary with electron energy as expected from quasi-linear theory. Based on quasi-linear theory, the pitch-angle diffusion rate $D_{\alpha\alpha,LC}$ of 60–300 keV electrons near $L^* = 6$ should vary like $\sim B_w^2/(\gamma p^{3/2})$, with B_w^2 the chorus wave power at the magnetic latitude λ of

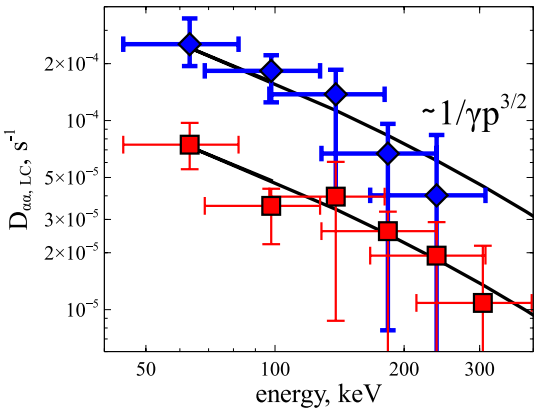

Figure 9. Variation of pitch-angle diffusion rates $D_{\alpha\alpha,LC}$ inferred from $J^{corr}_{precip}/J_{trapped}$ ratios obtained from Electron Loss and Fields Investigation (ELFIN) measurements near 9–10 MLT at $L^* = 6$ as a function of electron energy. Results on November 28 (9:10 UT) and November 7, 2020 (22:45 UT) are shown by red squares and blue diamonds, respectively. Error bars are calculated in the same way as in Figure 8b. The theoretical scaling law $D_{\alpha\alpha,LC} \sim 1/(\gamma p^{3/2})$ for a constant chorus wave power at latitudes $\sim 5° - 25°$ is shown by black curves.

cyclotron resonance (Aryan et al., 2020; Mourenas et al., 2012, 2014). Chorus wave statistics at $L^* \simeq 6$ (Agapitov et al., 2018; Aryan et al., 2020) show that B^2_w is nearly constant at 9–10 MLT over latitudes $\lambda = 5°–25°$ when AE < 300 nT, whereas B^2_w decreases by a factor ≈ 2 between $\lambda \sim 15°$ and $\lambda \sim 25°$ when $AE > 300$ nT. Therefore, $D_{\alpha\alpha,LC}$ should decrease approximately like $\sim 1/(\gamma p^{3/2})$ as electron energy increases from 60 to 300 keV when AE < 300 nT, and it should decrease slightly faster than $1/(\gamma p^{3/2})$ when AE > 300 nT.

Figure 9 shows the variation of inferred diffusion rates $D_{\alpha\alpha,LC}$ as a function of electron energy, for the same November 07 and November 28, 2020 cases investigated in Figure 8. The measured J_{up}/J_{precip} ratio is closer to 1 on November 28 than on November 07, leading to larger uncertainties on the estimated $J_{precip,\,corr}/J_{trapped} = (J_{precip} - J_{up})/J_{trapped}$. Nevertheless, Figure 9 shows that in both cases, the inferred diffusion rates $D_{\alpha\alpha,LC}$ vary approximately like $1/(\gamma p^{3/2})$ between 60 and 300 keV, as expected from quasi-linear theory. $D_{\alpha\alpha,LC}$ decreases slightly faster than $1/(\gamma p^{3/2})$ on 07 November, probably due to a more sensible decrease of chorus wave power B^2_w at $\lambda > 15°$, related to a larger $\langle SME \rangle$ during the two preceding hours than for the 28 November case (260 vs. 100 nT). These results further confirm the applicability of the quasi-linear theory, as well as the reliability of ELFIN electron flux measurements near and inside the loss cone for evaluating wave-driven pitch-angle diffusion rates.

3.5. Discussion

It is worth emphasizing that the presence of a significant amount of atmospheric backscatter (Davidson & Walt, 1977; Marshall & Bortnik, 2018; Selesnick et al., 2004) in both conjugate regions along a geomagnetic field line can translate into a background "noise level" of precipitated electron flux that should be subtracted from the measured total precipitated flux to get a reliable estimate of the fraction of electrons directly scattered into the loss cone by whistler-mode waves. ELFIN observations (see Figures 7 and 8 and Table 1) show that atmospheric backscatter indeed maintains a significant backscattered and precipitated electron flux inside the loss cone even during periods of weak wave-driven electron precipitation. Such electron populations are the remains of precipitated populations not yet fully lost, because of atmospheric backscatter. Without correcting for backscatter, instantaneous diffusion rates inferred from the measured total precipitated and trapped electron fluxes may therefore remain above an apparent lower limit fixed by atmospheric backscatter, which may vary with MLT, season, and geomagnetic activity (Picone et al., 2002).

Interestingly, a steeper decrease of the trapped electron flux toward higher energy may allow to infer lower or more accurate $D_{\alpha\alpha,LC}$ values from the measured precipitated to trapped electron flux ratio, because the relative contribution of backscattered flux (originating from higher energy precipitated electrons) to the measured precipitated electron flux should then be reduced (Marshall & Bortnik, 2018). Therefore, it would be interesting in the future to examine other periods during which trapped electrons exhibit a softer (steeper) energy spectrum.

What are the consequences of atmospheric backscatter on the lifetimes of trapped 100–200 keV electrons? Numerical simulations of atmospheric backscatter (Marshall & Bortnik, 2018; Selesnick et al., 2004) show that only $\approx 50 - 70\%$ of the precipitated electrons deep inside the loss cone, and only $\approx 10 - 20\%$ of the precipitated electrons close to α_{LC}, are fully lost in the atmosphere after $\Delta t \sim \tau_B/4$, contrary to the usual assumption of a 100% loss (Schulz & Lanzerotti, 1974). Nevertheless, practically all electrons inside the loss cone are still lost after $\Delta t \sim 3\tau_B \sim 3$ s, which represents a negligible delay compared with typical lifetimes $\tau_L > 1$ day and, therefore, should not affect theoretical lifetime estimates. Numerical simulations further show that a significant fraction of 100–200 keV electrons with initial $\alpha \in [\alpha_{LC}, 1.05\alpha_{LC}]$ should be precipitated, or backscattered inside the loss cone (Marshall & Bortnik, 2018). This slight increase of the effective loss cone angle α_{LC} should have a negligible impact on trapped electron lifetimes (Artemyev et al., 2013; Mourenas et al., 2012).

4. Conclusions

In the present paper, we used recent data from ELFIN CubeSats on low Earth orbit during three moderately disturbed periods in 2020, to comprehensively check the consistency between quasi-linear diffusion theory and observed electron flux variations. We found that instantaneous electron pitch-angle diffusion rates $D_{\alpha\alpha,LC}$, inferred using quasi-linear theory from ELFIN measurements of precipitated and trapped electron fluxes, are in good agreement with time-averaged theoretical diffusion rates based on statistical chorus wave models, provided that precipitated electron fluxes are appropriately corrected for atmospheric backscatter. Similarly, electron lifetimes τ_L independently derived from trapped electron flux decay observed by ELFIN over two to six days during the same periods are in good agreement with theoretical lifetimes from the statistical models, based on years-long statistics of hiss, chorus, and hydrogen-band EMIC waves (Aryan et al., 2020; Kersten et al., 2014; Li et al., 2015; Mourenas et al., 2016, 2017; Zhang et al., 2016). The pitch-angle distribution of precipitated electrons measured by ELFIN was also found to agree relatively well with the profile predicted by quasilinear theory.

Therefore, the present ELFIN results demonstrate for the first time a broad consistency between timescales of trapped electron flux decay, precipitated to trapped electron flux ratios, pitch-angle distributions inside the loss cone, and theoretical models of wave-driven electron quasi-linear diffusion. Although the present results are limited to several case studies, they suggest the reliability of quasi-linear theory for evaluating wave-driven electron diffusion toward the loss cone during moderately disturbed periods, and the reliability of statistical models of electron lifetimes parameterized by AE or *Kp* (Agapitov et al., 2020; Aryan et al., 2020; Mourenas et al., 2016, 2017) for evaluating electron precipitation into the atmosphere during not too disturbed periods. ELFIN data further show that the lifetimes of ∼1–3 MeV electrons can be reduced to $\tau_L \sim$ 1–2 days throughout the outer radiation belt (at $L^* \sim$ 4–6.5) in the aftermath of geomagnetic storms, in agreement with statistical lifetime models describing the combined effects of hydrogen-band EMIC waves and whistler-mode waves in different MLT sectors (Mourenas et al., 2016, 2017; Zhang et al., 2017). However, wave-driven pitch-angle diffusion (the only process taken into account in these electron lifetime models) is accompanied by energy diffusion, which may lead to electron acceleration (Horne & Thorne, 2003). This neglected phenomenon, together with radial diffusion by ULF waves (Ma et al., 2015; Ozeke et al., 2014), rapid electron injections from the plasma sheet (Turner et al., 2017), or non-linear effects from intense chorus waves (Gan et al., 2020; Hikishima et al., 2010), can modify the observed electron flux decay rates, or even lead to flux enhancements. Such neglected phenomena, which are much more present during disturbed periods (Ozeke et al., 2014; Zhang et al., 2018), probably explain some of the discrepancies between the observed and modeled flux decay rates. Therefore, all the above phenomena should be taken into account in large codes aiming at faithfully reproducing the observed electron flux dynamics, especially during disturbed and/or sufficiently long periods (>1 week).

In the near future, more work will be needed to fully assess the effects of atmospheric backscatter, and to analyze various other periods of trapped electron flux decay, especially during strongly disturbed times. More precise comparisons with quasilinear diffusion theory could be performed using numerical models of chorus wave-driven diffusion and atmospheric backscatter (Marshall & Bortnik, 2018; Selesnick et al., 2004; Tu et al., 2010). EMIC wave-driven electron loss will also be worth investigating using ELFIN simultaneous measurements of precipitated and trapped electron fluxes, to accurately determine the energy range of precipitation and examine uncertainties related to a possible presence of chorus wave-driven loss.

Appendix A: Anomalous Trapping by Chorus Wave Packets

During their rapid travel from the conjugate region to ELFIN, backscattered 100 keV electrons with small equatorial pitch-angle $\alpha < \alpha_{LC}$ may be sent outside the loss cone after resonant interaction with chorus waves, which tends to increase the pitch-angle of field-aligned resonant electrons (Inan et al., 1978; Lundin & Shkliar, 1977). This effect can potentially increase electron pitch-angle by a significant amount $\Delta\alpha > 0$, if electrons resonate with quasi-parallel chorus waves of sufficiently large magnetic amplitude to allow electron phase trapping (Albert et al., 2021; Artemyev et al., 2021; Kitahara & Katoh, 2019). Such intense waves can trap almost all small pitch-angle electrons and increase their pitch-angle, an effect called anomalous

trapping (Gan et al., 2020; Kitahara & Katoh, 2019). Whether field-aligned electrons within the loss cone will be transported to $\alpha > \alpha_{LC}$ or not, within a single resonant interaction, depends on the instantaneous wave amplitude at resonance and the wave packet size because the efficiency of phase trapping is significantly limited for short wave packets (Gan et al., 2020; Mourenas et al., 2018; Tao et al., 2013).

Time-weighted occurrences of chorus wave packets near $L^* \sim 6$ from Van Allen Probes statistics show that packets with peak amplitudes > 200 pT are present approximately ∼6% of the time when AE < 300 nT and ∼20% of the time when AE > 300 nT, while packets with peak amplitudes > 50 pT are present roughly ∼20% of the time when AE < 300 nT and ∼50% of the time when AE > 300 nT (Mourenas et al., 2018; Zhang et al., 2018, 2019).

Accordingly, we use test particle simulations (see numerical scheme details in Zhang, Agapitov, et al., 2020) to examine the nonlinear interaction of 100 keV electrons of small initial equatorial α with lower-band chorus wave packets of 50 and 200 pT peak amplitudes, with a typical frequency of 0.25 times the electron gyrofrequency (Agapitov et al., 2018). We assume either a constant peak wave amplitude at all latitudes, or a peak amplitude nearly constant up to a latitude of 20° and decreasing toward higher latitudes, as in chorus wave statistics (Agapitov et al., 2018; Aryan et al., 2020). We consider wave packets of length $\beta = +\infty$, $\beta = 15$, and $\beta = 5$, in number of wave periods. Most chorus wave packets observed at $L^* = 4.5$–6.5 are short, with $\beta \in [3, 15]$ (Mourenas et al., 2018; Zhang et al., 2019). The presence of large and random wave phase jumps between successive chorus packets generally allows to treat nonlinear resonant interactions with each wave packet independently (Zhang, Agapitov, et al., 2020; Zhang, Mourenas, et al., 2020). Therefore, we investigate electron interaction with one wave packet over half a bounce period at $L^* = 6$, where $\alpha_{LC} = 2.8°$. In the simulations, the initial electron pitch-angle distribution is taken as uniform over $\alpha \in [0.5°, 5°]$ to assess the net effect of anomalous trapping and nonlinear scattering (also called phase bunching), without significant quasi-linear diffusion effects (already taken into account in Equation 5 via the diffusion rate $D_{\alpha\alpha,LC}$). Indeed, such a uniform initial pitch-angle distribution should be left practically unchanged over $0.9° < \alpha < 2.8°$ by quasi-linear diffusion, which only works to reduce phase space density gradients (Kennel & Petschek, 1966) except close to $\alpha = 0°$ where pitch-angles can only increase.

Simulations results in Figures A1a, A1d, and A1g (dashed black and red curves) show that 50 pT wave packets have a too small amplitude to significantly reduce the number of loss cone electrons at $\alpha = 0.9°$–$2.8°$ via anomalous phase trapping (Albert et al., 2021; Artemyev et al., 2021), especially in the case of short packets with $\beta \simeq 5$–15 which represent the overwhelming majority (∼85%) of such packets (Mourenas et al., 2018; Zhang et al., 2019). Over half a bounce period, the average pitch-angle drift $\langle \Delta\alpha \rangle \sim 0.1°$ remains small, much smaller than scattering $\langle (\Delta\alpha)^2 \rangle^{1/2} \sim 0.5°$. Electrons initially just below $\alpha_{LC} = 2.8°$ and scattered, or trapped and transported, toward larger $\alpha > \alpha_{LC}$ are replaced by a nearly similar amount of electrons scattered from $\alpha > \alpha_{LC}$ to $\alpha < \alpha_{LC}$, leaving the loss cone electron distribution nearly unchanged.

In contrast, anomalous trapping by a very long 200 pT packet sends 90% of the electrons outside the loss cone, with an average pitch-angle increase of $\langle \Delta\alpha \rangle \sim 2°$–$4°$. Nonlinear scattering of electrons initially just outside the loss cone replaces only a small fraction of the expelled loss cone electrons (see dashed and solid blue curves in Figure A1a), resulting in a net ∼70% decrease of the number of loss cone electrons. However, chorus wave packets with >200 pT peak amplitudes represent only ∼30% of all packets with >50 pT peak amplitudes, and ∼85% have a short length $\beta < 15$ (Mourenas et al., 2018; Zhang et al., 2019). Simulations of electron interactions with such short 200 pT wave packets show that the reduced packet length diminishes the maximum duration of electron anomalous phase trapping (Gan et al., 2020), decreasing the pitch-angle drift $\langle \Delta\alpha \rangle$ by a factor of 2 as compared with $\beta = +\infty$ (see Figures A1d–A1i), similar to results obtained for usual phase trapping (Mourenas et al., 2018; Zhang, Agapitov, et al., 2020). Now, only ∼50% of the electrons are sent outside the loss cone by anomalous trapping, and part of them are replaced by electrons nonlinearly scattered from $\alpha > \alpha_{LC}$ to $\alpha < \alpha_{LC}$, leading to a net reduction of the loss cone distribution by only ∼30%.

Most of the time, however, backscattered electrons coming from the conjugate region will meet no intense resonant wave before reaching ELFIN and, thus, will remain inside the loss cone. Consequently, in the presence of a typical distribution of mostly short and low to moderate amplitude chorus wave packets (Mourenas et al., 2018; Zhang et al., 2019), nonlinear wave-particle interactions should not reduce the number of backscattered loss cone electrons at $\alpha = 0.9°$–$2.8°$ by more than ∼3%–7% during their rapid journey from

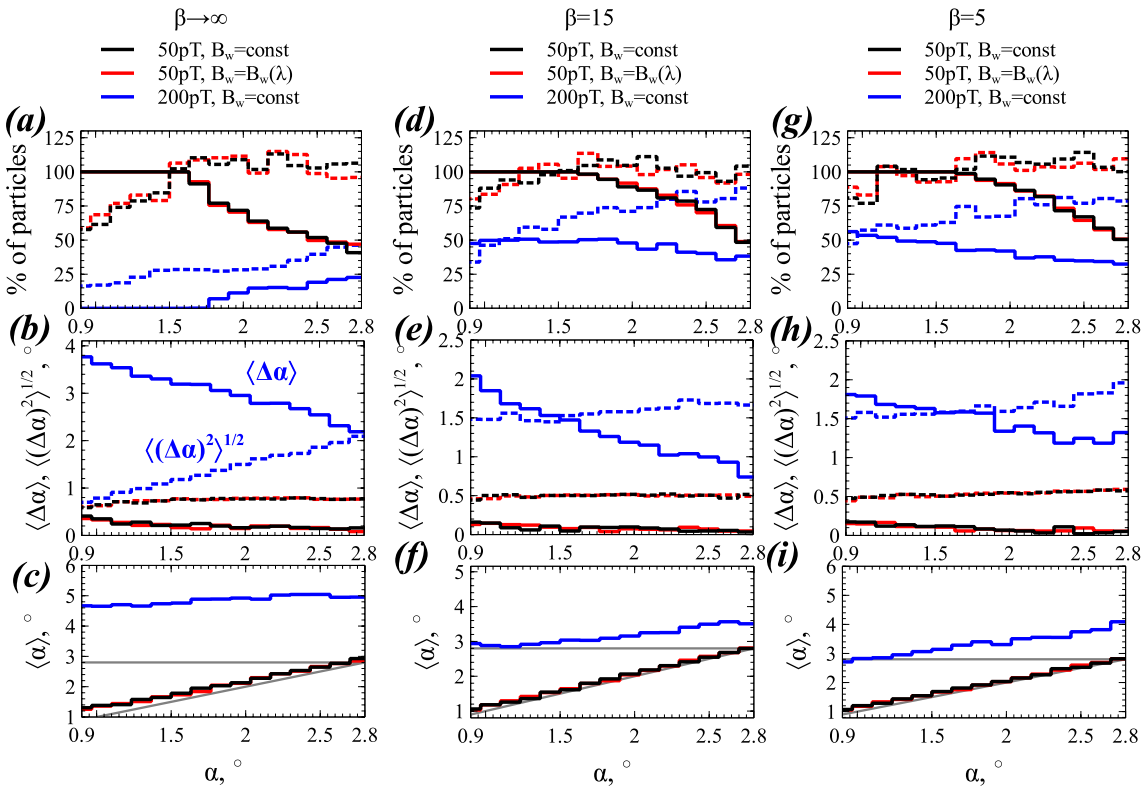

Figure A1. (a) Final percentage of electrons in each bin of $\alpha < \alpha_{LC} = 2.8°$ as compared with their initial number (dashed curves), and percentage of initial loss cone electrons remaining at $\alpha < \alpha_{LC}$ (solid curves), after one resonant interaction with a chorus wave packet, for a uniform initial electron pitch-angle distribution at $\alpha \in [0.5°, 5°]$. Results are shown for $\beta = +\infty$ wave packets of 50 pT peak amplitude constant at all latitudes (black curves) or with decreasing amplitude above 20° (red curves), and for packets of 200 pT peak amplitude constant at all latitudes (blue curves). (b) Average pitch-angle changes $\langle \Delta\alpha \rangle$ (solid curves) and $\langle (\Delta\alpha)^2 \rangle^{1/2}$ (dashed curves). (c) Average final α. (d, e, f) Same as (a, b, c) for short packets with $\beta = 15$. (g, h, i) Same as (a, b, c) for short packets with $\beta = 5$.

the conjugate region to ELFIN. A more detailed study of the effects of wave packet length on anomalous trapping is left for future work.

Data Availability Statement

ELFIN data is available at http://themis-data.igpp.ucla.edu/ela/. Data access and processing was done using SPEDAS V3.1, see Angelopoulos et al. (2019). The authors thank I.R. Mann, D.K. Milling and the rest of the CARISMA team for Pc1 wave data. CARISMA is operated by the University of Alberta, funded by the Canadian Space Agency. They gratefully acknowledge SuperMAG collaborators (https://supermag.jhuapl.edu/) for the SME index, and OMNI data available from the GSFC/SPDF OMNIWeb at https://omniweb.gsfc.nasa.gov.

Acknowledgments
X. J. Zhang, A. V. Artemyev, and V. Angelopoulos acknowledge support by NASA awards 80NSSC20K1270, NNX14AN68G, and NSF grants AGS-1242918, AGS-2019950, and AGS-2021749. The authors are grateful to NASA's CubeSat Launch Initiative for ELFIN's successful launch in the desired orbits. They acknowledge early support of ELFIN project by the AFOSR, under its University Nanosat Program, UNP-8 project, contract FA9453-12-D-0285, and by the California Space Grant program. They acknowledge critical contributions of numerous volunteer ELFIN team student members.

References

Abramowitz, M., & Stegun, I. A. (1972). In M. Abramowitz, & I. A. Stegun (Eds.), *Handbook of mathematical functions*.

Agapitov, O., Mourenas, D., Artemyev, A., Claudepierre, S. G., Hospodarsky, G., & Bonnell, J. W. (2020). Lifetimes of relativistic electrons as determined from plasmaspheric hiss scattering rates statistics: Effects of ω_{pe}/Ω_{ce} and wave frequency dependence on Geomagnetic Activity. *Geophysical Research Letters*, *47*, e2020GL088052. https://doi.org/10.1029/2020GL088052

Agapitov, O., Mourenas, D., Artemyev, A., Hospodarsky, G., & Bonnell, J. W. (2019). Time scales for electron quasi-linear diffusion by lower-band chorus waves: The effects of ω_{pe}/Ω_{ce} dependence on geomagnetic activity. *Geophysical Research Letters*, *46*(12), 6178–6187. https://doi.org/10.1029/2019GL083446

Agapitov, O. V., Artemyev, A., Krasnoselskikh, V., Khotyaintsev, Y. V., Mourenas, D., Breuillard, H., et al. (2013). Statistics of whistler mode waves in the outer radiation belt: Cluster STAFF-SA measurements. *Journal of Geophysical Research*, *118*, 3407–3420. https://doi.org/10.1002/jgra.50312

Agapitov, O. V., Artemyev, A. V., Mourenas, D., Kasahara, Y., & Krasnoselskikh, V. (2014). Inner belt and slot region electron lifetimes and energization rates based on AKEBONO statistics of whistler waves. *Journal of Geophysical Research*, *119*, 2876–2893. https://doi.org/10.1002/2014JA019886

Agapitov, O. V., Mourenas, D., Artemyev, A. V., Mozer, F. S., Hospodarsky, G., Bonnell, J., & Krasnoselskikh, V. (2018). Synthetic empirical chorus wave model from combined Van Allen Probes and cluster statistics. *Journal of Geophysical Research*, *123*(1), 297–314. https://doi.org/10.1002/2017JA024843

Albert, J. M., Artemyev, A. V., Li, W., Gan, L., & Ma, Q. (2021). Models of resonant wave-particle interactions. *Journal of Geophysical Research: Space Physics*, *126*, e2021JA029216. https://doi.org/10.1029/2021JA029216

Albert, J. M., & Shprits, Y. Y. (2009). Estimates of lifetimes against pitch angle diffusion. *Journal of Atmospheric and Solar-Terrestrial Physics*, *71*, 1647–1652. https://doi.org/10.1016/j.jastp.2008.07.004

Angelopoulos, V., Cruce, P., Drozdov, A., Grimes, E. W., Hatzigeorgiu, N., King, D. A., & Schroeder, P. (2019). The space physics environment data analysis system (SPEDAS). *Space Science Reviews*, *215*. https://doi.org/10.1007/s11214-018-0576-4

Angelopoulos, V., Tsai, E., Bingley, L., Shaffer, C., Turner, D. L., Runov, A., & Zhang, G. Y. (2020). The ELFIN Mission. *Space Science Reviews*, *216*(5), 103. https://doi.org/10.1007/s11214-020-00721-7

Artemyev, A. V., Agapitov, O., Mourenas, D., Krasnoselskikh, V., Shastun, V., & Mozer, F. (2016). Oblique whistler-mode waves in the Earth's inner magnetosphere: Energy distribution, origins, and role in radiation belt dynamics. *Space Science Reviews*, *200*(1–4), 261–355. https://doi.org/10.1007/s11214-016-0252-5

Artemyev, A. V., Mourenas, D., Agapitov, O. V., & Krasnoselskikh, V. V. (2013). Parametric validations of analytical lifetime estimates for radiation belt electron diffusion by whistler waves. *Annales Geophysicae*, *31*, 599–624. https://doi.org/10.5194/angeo-31-599-2013

Artemyev, A. V., Neishtadt, A. I., Albert, J. M., Gan, L., Li, W., & Ma, Q. (2021). Theoretical model of the nonlinear resonant interaction of whistler-mode waves and field-aligned electrons. *Physics of Plasmas*, *28*(5), 052902. https://doi.org/10.1063/5.0046635

Aryan, H., Agapitov, O. V., Artemyev, A., Mourenas, D., Balikhin, M. A., Boynton, R., & Bortnik, J. (2020). Outer radiation belt electron lifetime model based on combined Van Allen Probes and cluster VLF measurements. *Journal of Geophysical Research: Space Physics*, *125*(8), e28018. https://doi.org/10.1029/2020JA028018

Baker, D. N., Jaynes, A. N., Li, X., Henderson, M. G., Kanekal, S. G., Reeves, G. D., & Shprits, Y. Y. (2014). Gradual diffusion and punctuated phase space density enhancements of highly relativistic electrons: Van Allen Probes observations. *Geophysical Research Letters*, *41*, 1351–1358. https://doi.org/10.1002/2013GL058942

Blum, L. W., Halford, A., Millan, R., Bonnell, J. W., Goldstein, J., Usanova, M., & Li, X. (2015). Observations of coincident EMIC wave activity and duskside energetic electron precipitation on 18-19 January 2013. *Geophysical Research Letters*, *42*, 5727–5735. https://doi.org/10.1002/2015GL065245

Boyd, A. J., Spence, H. E., Claudepierre, S. G., Fennell, J. F., Blake, J. B., Baker, D. N., & Turner, D. L. (2014). Quantifying the radiation belt seed population in the 17 March 2013 electron acceleration event. *Geophysical Research Letters*, *41*, 2275–2281. https://doi.org/10.1002/2014GL059626

Boynton, R. J., Mourenas, D., & Balikhin, M. A. (2016). Electron flux dropouts at Geostationary Earth Orbit: Occurrences, magnitudes, and main driving factors. *Journal of Geophysical Research: Space Physics*, *121*, 8448–8461. https://doi.org/10.1002/2016JA022916

Boynton, R. J., Mourenas, D., & Balikhin, M. A. (2017). Electron flux dropouts at $L \sim 4.2$ from global positioning system satellites: Occurrences, magnitudes, and main driving factors. *Journal of Geophysical Research: Space Physics*, *122*(11), 11428–11441. https://doi.org/10.1002/2017JA024523

Breneman, A. W., Halford, A., Millan, R., McCarthy, M., Fennell, J., Sample, J., & Kletzing, C. A. (2015). Global-scale coherence modulation of radiation-belt electron loss from plasmaspheric hiss. *Nature*, *523*, 193–195. https://doi.org/10.1038/nature14515

Chen, L., Breneman, A. W., Xia, Z., & Zhang, X.-j. (2020). Modeling of bouncing electron microbursts induced by ducted chorus waves. *Geophysical Research Letters*, *47*(17), e89400. https://doi.org/10.1029/2020GL089400

Chen, L., Thorne, R. M., Jordanova, V. K., Wang, C.-P., Gkioulidou, M., Lyons, L., & Horne, R. B. (2010). Global simulation of EMIC wave excitation during the 21 April 2001 storm from coupled RCM-RAM-HOTRAY modeling. *Journal of Geophysical Research*, *115*(A7), A07209. https://doi.org/10.1029/2009JA015075

Claudepierre, S. G., Ma, Q., Bortnik, J., O'Brien, T. P., Fennell, J. F., & Blake, J. B. (2020). Empirically estimated electron lifetimes in the earth's radiation belts: Comparison with theory. *Geophysical Research Letters*, *47*(3), e86056. https://doi.org/10.1029/2019GL086056

Davidson, R. C., & Walt, M. (1977). Loss cone distributions of radiation belt electrons. *Journal of Geophysical Research*, *82*, 48–54. https://doi.org/10.1029/JA082i001p00048

Fukushima, T. (2013). Precise and fast computation of Lambert functions without transcendental function evaluations. *Journal of Computational and Applied Mathematics*, *244*, 77–89. https://doi.org/10.1016/j.cam.2012.11.021

Gan, L., Li, W., Ma, Q., Albert, J. M., Artemyev, A. V., & Bortnik, J. (2020). Nonlinear interactions between radiation belt electrons and chorus waves: Dependence on wave amplitude modulation. *Geophysical Research Letters*, *47*(4), e85987. https://doi.org/10.1029/2019GL085987

Gao, X., Li, W., Thorne, R. M., Bortnik, J., Angelopoulos, V., Lu, Q., & Wang, S. (2014). Statistical results describing the bandwidth and coherence coefficient of whistler mode waves using THEMIS waveform data. *Journal of Geophysical Research*, *119*, 8992–9003. https://doi.org/10.1002/2014JA020158

Gjerloev, J. W. (2012). The SuperMAG data processing technique. *Journal of Geophysical Research*, *117*, A09213. https://doi.org/10.1029/2012JA017683

Glauert, S. A., Horne, R. B., & Meredith, N. P. (2014). Three-dimensional electron radiation belt simulations using the BAS Radiation Belt Model with new diffusion models for chorus, plasmaspheric hiss, and lightning-generated whistlers. *Journal of Geophysical Research*, *119*, 268–289. https://doi.org/10.1002/2013JA019281

Grach, V. S., & Demekhov, A. G. (2020). Precipitation of relativistic electrons under resonant interaction with electromagnetic ion cyclotron wave packets. *Journal of Geophysical Research: Space Physics*, *125*(2), e27358. https://doi.org/10.1029/2019JA027358

He, Z., Yu, J., Li, K., Liu, N., Chen, Z., & Cui, J. (2021). A comparative study on the distributions of incoherent and coherent plasmaspheric hiss. *Geophysical Research Letters*, *48*, e2021GL092902. https://doi.org/10.1029/2021GL092902

Hikishima, M., Omura, Y., & Summers, D. (2010). Microburst precipitation of energetic electrons associated with chorus wave generation. *Geophysical Research Letters*, *37*, L07103. https://doi.org/10.1029/2010GL042678

Horne, R. B., & Thorne, R. M. (2003). Relativistic electron acceleration and precipitation during resonant interactions with whistler-mode chorus. *Geophysical Research Letters*, *30*(10), 1527. https://doi.org/10.1029/2003GL016973

Inan, U. S., Bell, T. F., & Helliwell, R. A. (1978). Nonlinear pitch angle scattering of energetic electrons by coherent VLF waves in the magnetosphere. *Journal of Geophysical Research*, *83*(A7), 3235–3254. https://doi.org/10.1029/JA083iA07p03235

Kennel, C. F., & Petschek, H. E. (1966). Limit on stably trapped particle fluxes. *Journal of Geophysical Research*, *71*, 1–28. https://doi.org/10.1029/jz071i001p00001

Kersten, T., Horne, R. B., Glauert, S. A., Meredith, N. P., Fraser, B. J., & Grew, R. S. (2014). Electron losses from the radiation belts caused by EMIC waves. *Journal of Geophysical Research*, *119*, 8820–8837. https://doi.org/10.1002/2014JA020366

Kim, H.-J., & Chan, A. A. (1997). Fully adiabatic changes in storm time relativistic electron fluxes. *Journal of Geophysical Research*, *102*, 22107–22116. https://doi.org/10.1029/97JA01814

Kitahara, M., & Katoh, Y. (2019). Anomalous trapping of low pitch angle electrons by coherent whistler mode waves. *Journal of Geophysical Research*, *124*(7), 5568–5583. https://doi.org/10.1029/2019JA026493

Li, W., Bortnik, J., Thorne, R. M., & Angelopoulos, V. (2011). Global distribution of wave amplitudes and wave normal angles of chorus waves using THEMIS wave observations. *Journal of Geophysical Research*, *116*, 12205. https://doi.org/10.1029/2011JA017035

Li, W., Ma, Q., Thorne, R. M., Bortnik, J., Kletzing, C. A., Kurth, W. S., & Nishimura, Y. (2015). Statistical properties of plasmaspheric hiss derived from Van Allen Probes data and their effects on radiation belt electron dynamics. *Journal of Geophysical Research*, *120*, 3393–3405. https://doi.org/10.1002/2015JA021048

Li, W., Ni, B., Thorne, R. M., Bortnik, J., Green, J. C., Kletzing, C. A., & Hospodarsky, G. B. (2013). Constructing the global distribution of chorus wave intensity using measurements of electrons by the POES satellites and waves by the Van Allen Probes. *Geophysical Research Letters*, *40*, 4526–4532. https://doi.org/10.1002/grl.50920

Li, W., Shprits, Y. Y., & Thorne, R. M. (2007). Dynamic evolution of energetic outer zone electrons due to wave-particle interactions during storms. *Journal of Geophysical Research*, *112*, A10220. https://doi.org/10.1029/2007JA012368

Li, W., Thorne, R. M., Nishimura, Y., Bortnik, J., Angelopoulos, V., McFadden, J. P., & Auster, U. (2010). THEMIS analysis of observed equatorial electron distributions responsible for the chorus excitation. *Journal of Geophysical Research*, *115*, A00F11. https://doi.org/10.1029/2009JA014845

Liu, N., Su, Z., Gao, Z., Zheng, H., Wang, Y., Wang, S., & Matsuoka, A. (2020). Comprehensive observations of substorm enhanced plasmaspheric hiss generation, propagation and dissipation. *Geophysical Research Letters*, *47*(2), e2019GL086040. https://doi.org/10.1029/2019GL086040

Lundin, B. V., & Shkliar, D. R. (1977). Interaction of electrons with low transverse velocities with VLF waves in an inhomogeneous plasma. *Geomagnetism and Aeronomy*, *17*, 246–251.

Lyons, L. R., & Thorne, R. M. (1973). Equilibrium structure of radiation belt electrons. *Journal of Geophysical Research*, *78*, 2142–2149. https://doi.org/10.1029/JA078i013p02142

Ma, Q., Li, W., Thorne, R. M., Ni, B., Kletzing, C. A., Kurth, W. S., & Angelopoulos, V. (2015). Modeling inward diffusion and slow decay of energetic electrons in the Earth's outer radiation belt. *Geophysical Research Letters*, *42*, 987–995. https://doi.org/10.1002/2014GL062977

Ma, Q., Mourenas, D., Li, W., Artemyev, A., & Thorne, R. M. (2017). VLF waves from ground-based transmitters observed by the Van Allen Probes: Statistical model and effects on plasmaspheric electrons. *Geophysical Research Letters*, *44*, 6483–6491. https://doi.org/10.1002/2017GL073885

Malaspina, D. M., Jaynes, A. N., Boulé, C., Bortnik, J., Thaller, S. A., Ergun, R. E., et al. (2016). The distribution of plasmaspheric hiss wave power with respect to plasmapause location. *Geophysical Research Letters*, *43*, 7878–7886. https://doi.org/10.1002/2016GL069982

Marshall, R. A., & Bortnik, J. (2018). Pitch angle dependence of energetic electron precipitation: Energy deposition, backscatter, and the bounce loss cone. *Journal of Geophysical Research*, *123*, 2412–2423. https://doi.org/10.1002/2017JA024873

Meredith, N. P., Horne, R. B., & Anderson, R. R. (2001). Substorm dependence of chorus amplitudes: Implications for the acceleration of electrons to relativistic energies. *Journal of Geophysical Research*, *106*, 13165–13178. https://doi.org/10.1029/2000JA900156

Meredith, N. P., Horne, R. B., Glauert, S. A., Baker, D. N., Kanekal, S. G., & Albert, J. M. (2009). Relativistic electron loss timescales in the slot region. *Journal of Geophysical Research*, *114*, A03222. https://doi.org/10.1029/2008JA013889

Mourenas, D., Artemyev, A. V., Agapitov, O. V., & Krasnoselskikh, V. (2014). Consequences of geomagnetic activity on energization and loss of radiation belt electrons by oblique chorus waves. *Journal of Geophysical Research*, *119*, 2775–2796. https://doi.org/10.1002/2013JA019674

Mourenas, D., Artemyev, A. V., Ma, Q., Agapitov, O. V., & Li, W. (2016). Fast dropouts of multi-MeV electrons due to combined effects of EMIC and whistler mode waves. *Geophysical Research Letters*, *43*(9), 4155–4163. https://doi.org/10.1002/2016GL068921

Mourenas, D., Artemyev, A. V., Ripoll, J.-F., Agapitov, O. V., & Krasnoselskikh, V. V. (2012). Timescales for electron quasi-linear diffusion by parallel and oblique lower-band Chorus waves. *Journal of Geophysical Research*, *117*, A06234. https://doi.org/10.1029/2012JA017717

Mourenas, D., Artemyev, A. V., & Zhang, X.-J. (2019). Impact of significant time-integrated geomagnetic activity on 2-MeV electron flux. *Journal of Geophysical Research: Space Physics*, *124*, 4445–4461. https://doi.org/10.1029/2019JA026659

Mourenas, D., Ma, Q., Artemyev, A. V., & Li, W. (2017). Scaling laws for the inner structure of the radiation belts. *Geophysical Research Letters*, *44*, 3009–3018. https://doi.org/10.1002/2017GL072987

Mourenas, D., Zhang, X.-J., Artemyev, A. V., Angelopoulos, V., Thorne, R. M., Bortnik, J., & Vasiliev, A. A. (2018). Electron nonlinear resonant interaction with short and intense parallel chorus wave packets. *Journal of Geophysical Research*, *123*, 4979–4999. https://doi.org/10.1029/2018JA025417

Mozer, F. S., Agapitov, O. V., Blake, J. B., & Vasko, I. Y. (2018). Simultaneous observations of lower band chorus emissions at the equator and microburst precipitating electrons in the ionosphere. *Geophysical Research Letters*, *45*, 511–516. https://doi.org/10.1002/2017GL076120

Murphy, K. R., Watt, C. E. J., Mann, I. R., Rae, I. J., Sibeck, D. G., Boyd, A. J., & Fennell, J. (2018). The global statistical response of the outer radiation belt during geomagnetic storms. *Geophysical Research Letters*, *45*, 3783–3792. https://doi.org/10.1002/2017GL076674

Newell, P. T., & Gjerloev, J. W. (2011). Evaluation of SuperMAG auroral electrojet indices as indicators of substorms and auroral power. *Journal of Geophysical Research*, *116*, A12211. https://doi.org/10.1029/2011JA016779

Ni, B., Cao, X., Zou, Z., Zhou, C., Gu, X., Bortnik, J., & Xie, L. (2015). Resonant scattering of outer zone relativistic electrons by multiband EMIC waves and resultant electron loss time scales. *Journal of Geophysical Research*, *120*, 7357–7373. https://doi.org/10.1002/2015JA021466

Ni, B., Thorne, R. M., Shprits, Y. Y., & Bortnik, J. (2008). Resonant scattering of plasma sheet electrons by whistler-mode chorus: Contribution to diffuse auroral precipitation. *Geophysical Research Letters*, *35*, L11106. https://doi.org/10.1029/2008GL034032

O'Brien, T. P., & Moldwin, M. B. (2003). Empirical plasmapause models from magnetic indices. *Geophysical Research Letters*, *30*(4), 1152. https://doi.org/10.1029/2002GL016007

Olifer, L., Mann, I. R., Boyd, A. J., Ozeke, L. G., & Choi, D. (2018). On the role of last closed drift shell dynamics in driving fast losses and Van Allen radiation belt extinction. *Journal of Geophysical Research*, *123*, 3692–3703. https://doi.org/10.1029/2018JA025190

Omura, Y., Katoh, Y., & Summers, D. (2008). Theory and simulation of the generation of whistler-mode chorus. *Journal of Geophysical Research*, *113*, A04223. https://doi.org/10.1029/2007JA012622

Ozeke, L. G., Mann, I. R., Murphy, K. R., Jonathan Rae, I., & Milling, D. K. (2014). Analytic expressions for ULF wave radiation belt radial diffusion coefficients. *Journal of Geophysical Research*, *119*, 1587–1605. https://doi.org/10.1002/2013JA019204

Ozhogin, P., Tu, J., Song, P., & Reinisch, B. W. (2012). Field-aligned distribution of the plasmaspheric electron density: An empirical model derived from the IMAGE RPI measurements. *Journal of Geophysical Research*, *117*, A06225. https://doi.org/10.1029/2011JA017330

Pettit, J. M., Randall, C. E., Peck, E. D., Marsh, D. R., van de Kamp, M., Fang, X., & Funke, B. (2019). Atmospheric effects of >30-keV energetic electron precipitation in the southern hemisphere winter during 2003. *Journal of Geophysical Research*, *124*, 8138–8153. https://doi.org/10.1029/2019JA026868

Picone, J. M., Hedin, A. E., Drob, D. P., & Aikin, A. C. (2002). NRLMSISE-00 empirical model of the atmosphere: Statistical comparisons and scientific issues. *Journal of Geophysical Research*, *107*(A12), 1468. https://doi.org/10.1029/2002JA009430

Pinto, V. A., Mourenas, D., Bortnik, J., Zhang, X.-J., Artemyev, A. V., Moya, P. S., & Lyons, L. R. (2019). Decay of ultra-relativistic remnant belt electrons through scattering by plasmaspheric hiss. *Journal of Geophysical Research*, *124*, 5222–5233. https://doi.org/10.1029/2019JA026509

Pinto, V. A., Zhang, X.-J., Mourenas, D., Bortnik, J., Artemyev, A. V., Lyons, L. R., & Moya, P. S. (2020). On the confinement of ultrarelativistic electron remnant belts to low L shells. *Journal of Geophysical Research*, *125*, e27469. https://doi.org/10.1029/2019JA027469

Reidy, J. A., Horne, R. B., Glauert, S. A., Clilverd, M. A., Meredith, N. P., Woodfield, E. E., & Rodger, C. J. (2021). Comparing electron precipitation fluxes calculated from pitch angle diffusion coefficients to LEO satellite observations. *Journal of Geophysical Research*, *126*, e2020JA028410. https://doi.org/10.1029/2020JA028410

Ross, J. P. J., Meredith, N. P., Glauert, S. A., Horne, R. B., & Clilverd, M. A. (2019). Effects of VLF transmitter waves on the inner belt and slot region. *Journal of Geophysical Research: Space Physics*, *124*(7), 5260–5277. https://doi.org/10.1029/2019JA026716

Sandanger, M., Søraas, F., Aarsnes, K., Oksavik, K., & Evans, D. S. (2007). Loss of relativistic electrons: Evidence for pitch angle scattering by electromagnetic ion cyclotron waves excited by unstable ring current protons. *Journal of Geophysical Research*, *112*, A12213. https://doi.org/10.1029/2006JA012138

Schulz, M., & Lanzerotti, L. J. (1974). *Particle diffusion in the radiation belts*. Springer.

Selesnick, R. S., Looper, M. D., & Albert, J. M. (2004). Low-altitude distribution of radiation belt electrons. *Journal of Geophysical Research*, *109*(A11), A11209. https://doi.org/10.1029/2004JA010611

Seppälä, A., Douma, E., Rodger, C. J., Verronen, P. T., Clilverd, M. A., & Bortnik, J. (2018). Relativistic electron microburst events: Modeling the atmospheric impact. *Geophysical Research Letters*, *45*, 1141–1147. https://doi.org/10.1002/2017GL075949

Sheeley, B. W., Moldwin, M. B., Rassoul, H. K., & Anderson, R. R. (2001). An empirical plasmasphere and trough density model: CRRES observations. *Journal of Geophysical Research*, *106*, 25631–25642. https://doi.org/10.1029/2000JA000286

Shprits, Y. Y., Thorne, R. M., Friedel, R., Reeves, G. D., Fennell, J., Baker, D. N., & Kanekal, S. G. (2006). Outward radial diffusion driven by losses at magnetopause. *Journal of Geophysical Research*, *111*, A11214. https://doi.org/10.1029/2006JA011657

Simms, L. E., Engebretson, M. J., Clilverd, M. A., Rodger, C. J., & Reeves, G. D. (2018). Nonlinear and synergistic effects of ULF Pc5, VLF chorus, and EMIC waves on relativistic electron flux at geosynchronous orbit. *Journal of Geophysical Research: Space Physics*, *123*, 4755–4766. https://doi.org/10.1029/2017JA025003

Su, Z., Gao, Z., Zhu, H., Li, W., Zheng, H., Wang, Y., & Wygant, J. R. (2016). Nonstorm time dropout of radiation belt electron fluxes on 24 September 2013. *Journal of Geophysical Research*, *121*, 6400–6416. https://doi.org/10.1002/2016JA022546

Summers, D., & Thorne, R. M. (2003). Relativistic electron pitch-angle scattering by electromagnetic ion cyclotron waves during geomagnetic storms. *Journal of Geophysical Research*, *108*(A4), 1143. https://doi.org/10.1029/2002JA009489

Tao, X., Bortnik, J., Albert, J. M., & Thorne, R. M. (2012). Comparison of bounce-averaged quasi-linear diffusion coefficients for parallel propagating whistler mode waves with test particle simulations. *Journal of Geophysical Research*, *117*, A10205. https://doi.org/10.1029/2012JA017931

Tao, X., Bortnik, J., Albert, J. M., Thorne, R. M., & Li, W. (2013). The importance of amplitude modulation in nonlinear interactions between electrons and large amplitude whistler waves. *Journal of Atmospheric and Solar-Terrestrial Physics*, *99*, 67–72. https://doi.org/10.1016/j.jastp.2012.05.012

Thorne, R. M., & Kennel, C. F. (1971). Relativistic electron precipitation during magnetic storm main phase. *Journal of Geophysical Research*, *76*, 4446–4453. https://doi.org/10.1029/JA076i019p04446

Thorne, R. M., Li, W., Ni, B., Ma, Q., Bortnik, J., Chen, L., & Kanekal, S. G. (2013). Rapid local acceleration of relativistic radiation-belt electrons by magnetospheric chorus. *Nature*, *504*, 411–414. https://doi.org/10.1038/nature12889

Tsurutani, B. T., & Smith, E. J. (1977). Two types of magnetospheric ELF chorus and their substorm dependences. *Journal of Geophysical Research*, *82*, 5112–5128. https://doi.org/10.1029/JA082i032p05112

Tu, W., Selesnick, R., Li, X., & Looper, M. (2010). Quantification of the precipitation loss of radiation belt electrons observed by SAMPEX. *Journal of Geophysical Research*, *115*, A07210. https://doi.org/10.1029/2009JA014949

Turner, D. L., Angelopoulos, V., Li, W., Bortnik, J., Ni, B., Ma, Q., & Rodriguez, J. V. (2014). Competing source and loss mechanisms due to wave-particle interactions in Earth's outer radiation belt during the 30 September to 3 October 2012 geomagnetic storm. *Journal of Geophysical Research*, *119*, 1960–1979. https://doi.org/10.1002/2014JA019770

Turner, D. L., Fennell, J. F., Blake, J. B., Claudepierre, S. G., Clemmons, J. H., Jaynes, A. N., & Reeves, G. D. (2017). Multipoint observations of energetic particle injections and substorm activity during a conjunction between magnetospheric multiscale (MMS) and Van Allen Probes. *Journal of Geophysical Research: Space Physics*, *122*(1111), 11481–11504. https://doi.org/10.1002/2017JA024554

Turner, D. L., O'Brien, T. P., Fennell, J. F., Claudepierre, S. G., Blake, J. B., Kilpua, E., & Hietala, H. (2015). The effects of geomagnetic storms on electrons in Earth's radiation belts. *Geophysical Research Letters*, *42*(21), 9176–9184. https://doi.org/10.1002/2015GL064747

Usanova, M. E., Drozdov, A., Orlova, K., Mann, I. R., Shprits, Y., Robertson, M. T., & Wygant, J. (2014). Effect of EMIC waves on relativistic and ultrarelativistic electron populations: Ground-based and Van Allen Probes observations. *Geophysical Research Letters*, *41*, 1375–1381. https://doi.org/10.1002/2013GL059024

Zhang, X. J., Agapitov, O., Artemyev, A. V., Mourenas, D., Angelopoulos, V., Kurth, W. S., & Hospodarsky, G. B. (2020). Phase decoherence within intense chorus wave packets constrains the efficiency of nonlinear resonant electron acceleration. *Geophysical Research Letters*, *47*(20), e89807. https://doi.org/10.1029/2020GL089807

Zhang, X.-J., Li, W., Thorne, R. M., Angelopoulos, V., Bortnik, J., Kletzing, C. A., & Hospodarsky, G. B. (2016). Statistical distribution of EMIC wave spectra: Observations from Van Allen Probes. *Geophysical Research Letters*, *43*(2412), 12348–12355. https://doi.org/10.1002/2016GL071158

Zhang, X. J., Mourenas, D., Artemyev, A. V., Angelopoulos, V., Bortnik, J., Thorne, R. M., & Hospodarsky, G. B. (2019). Nonlinear electron interaction with intense chorus waves: Statistics of occurrence rates. *Geophysical Research Letters*, *46*(13), 7182–7190. https://doi.org/10.1029/2019GL083833

Zhang, X. J., Mourenas, D., Artemyev, A. V., Angelopoulos, V., Kurth, W. S., Kletzing, C. A., & Hospodarsky, G. B. (2020). Rapid frequency variations within intense chorus wave packets. *Geophysical Research Letters*, *47*(15), e88853. https://doi.org/10.1029/2020GL088853

Zhang, X.-J., Mourenas, D., Artemyev, A. V., Angelopoulos, V., & Thorne, R. M. (2017). Contemporaneous EMIC and whistler mode waves: Observations and consequences for MeV electron loss. *Geophysical Research Letters*, *44*, 8113–8121. https://doi.org/10.1002/2017GL073886

Zhang, X.-J., Mourenas, D., Shen, X.-C., Qin, M., Artemyev, A. V., Ma, Q., & Angelopoulos, V. (2021). Dependence of relativistic electron precipitation in the ionosphere on EMIC wave minimum resonant energy at the conjugate equator. *Journal of Geophysical Research*, *126*(5), e2021JA029193. https://doi.org/10.1029/2021JA029193

Zhang, X. J., Thorne, R., Artemyev, A., Mourenas, D., Angelopoulos, V., Bortnik, J., & Hospodarsky, G. B. (2018). Properties of intense field-aligned lower-band chorus waves: Implications for nonlinear wave-particle interactions. *Journal of Geophysical Research: Space Physics*, *123*(7), 5379–5393. https://doi.org/10.1029/2018JA025390

Zhou, C., Yang, G., Ni, B., Zhao, Z., Hu, Z.-J., & Shi, R. (2013). Strong diffusion limit in the realistic magnetosphere: Dependence on geomagnetic condition and spatial location. *Journal of Geophysical Research*, *118*(1), 118–131. https://doi.org/10.1029/2012JA018207